Cancer Biol Med 2025. doi: 10.20892/j.issn.2095-3941.2025.0275

ORIGINAL ARTICLE

# Nintedanib enhances tumor cell radiosensitivity by promoting ferroptosis and modulating the ATF4/SLC7A11/GSH axis

Chunya Li, Aifeina Aili, Qingqing Yu, Mu Yang, Qiyuan Feng, Duo Xu, Bo Liu, Jingyao Tu, Xianglin Yuan
Department of Oncology, Tongji Hospital, Tongji Medical College, Huazhong University of Science and Technology, Wuhan 430030, China

**ABSTRACT**

**Objective:** Tumor cell radio-resistance and radiation-induced fibrosis of normal tissues hinder the efficacy of radiotherapy. Nintedanib, a promising therapeutic agent for radiation-induced pulmonary fibrosis and solid tumors, has yet to be investigated in combination with radiotherapy. This study aimed to evaluate the antitumor efficacy of nintedanib in conjunction with radiotherapy.
**Methods:** Tumor-bearing models were utilized to assess the antitumor effects and safety of treatment with nintedanib and radiotherapy *in vivo*. Reactive oxygen species (ROS), lipid peroxidation assays, and transmission electron microscopy were used to determine the impact of the combined treatment strategy on tumor cell death. Overexpression plasmids and shRNA knockdown techniques were applied to explore and validate the underlying mechanisms.
**Results:** The combination of nintedanib and radiotherapy demonstrated a potent antitumor effect *in vivo*. Nintedanib suppressed the SLC7A11-mediated GSH synthesis pathway by downregulating ATF4, the expression of which was elevated in response to radiation as an adaptive mechanism. Consequently, nintedanib combined with radiotherapy enhanced ferroptosis in tumor cells.
**Conclusion:** These findings support the use of nintedanib in combination with radiotherapy as an effective, low-toxicity treatment strategy, highlighting the antitumor potential of ATF4-targeted agents.

**KEYWORDS** Nintedanib; radiotherapy; ferroptosis; ATF4; SLC7A11

## Introduction

Cancer, a public health challenge, accounts for one in four deaths (22.8%) from non-communicable diseases globally. Radiotherapy (RT) has a critical role in both definitive and palliative treatment across various stages of solid tumors[1-4]. Nevertheless, cancers that have undergone RT still have a considerable recurrence rate, which is approximately 5.2%, 55%, 4.31%, 6.5%, and 50%–60% in head and neck tumors[5], cervical cancer[6], breast cancer[7], rectal cancer[8,9], and locally advanced non-small cell lung cancer[10,11], respectively. The efficacy of RT is hindered by tumor cell resistance to radiation and the collateral damage to normal tissues, such as radiation-induced esophageal, pulmonary, and gastrointestinal damage[12-16]. Therefore, developing effective, low-toxicity strategies to improve RT outcomes is crucial.

Nintedanib, a multitarget tyrosine kinase inhibitor, has been approved for the treatment of idiopathic pulmonary fibrosis[17] and non-small cell lung cancer that has progressed following first-line chemotherapy[18]. A phase II clinical study showed that nintedanib prophylactically reduced the incidence of radiation pneumonia in patients with non-small cell lung cancer undergoing chemo-RT[19]. Our prior work also indicated that nintedanib administered 2 days before or 4 weeks after thoracic RT significantly reduced lung collagen deposition and improved overall health in mice[20]. Clinical trials have highlighted the advantages of nintedanib combined with chemotherapy over other anti-angiogenic therapies in solid tumors, such as ovarian cancer, colorectal cancer, non-small cell lung cancer, and hepatocellular carcinoma[21-25]. Preclinical studies further demonstrated substantial antitumor efficacy when

Correspondence to: Jingyao Tu and Xianglin Yuan
E-mail: tujingyao@tjh.tjmu.edu.cn and yuanxianglin@hust.edu.cn
ORCID ID: https://orcid.org/0009-0003-7313-1298 and https://orcid.org/0000-0003-4653-5388
Received May 30, 2025; accepted August 27, 2025;
published online November 19, 2025.
Available at www.cancerbiomed.org
©2025 The Authors. Creative Commons Attribution-NonCommercial 4.0 International License

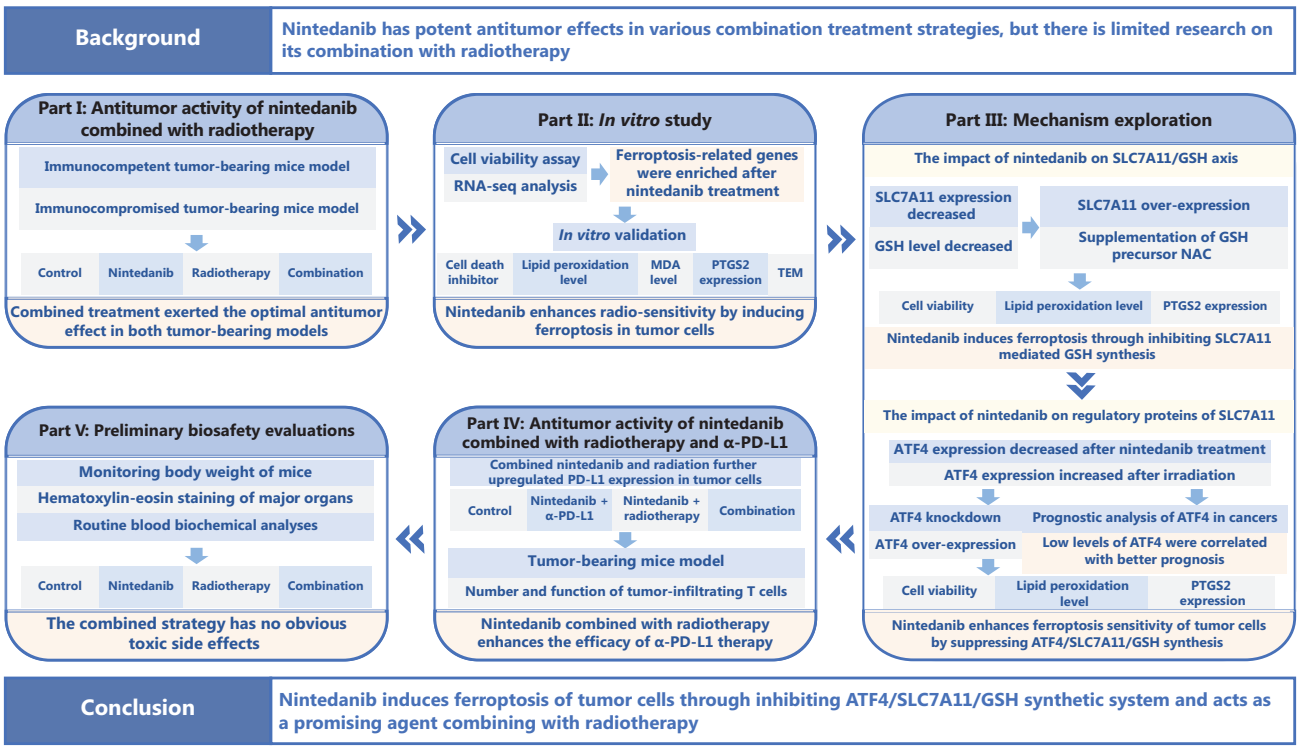


**Study flowchart** Part I explored the antitumor efficacy of nintedanib combined with radiotherapy in tumor-bearing immunocompromised mice models and tumor-bearing immunocompetent mice models. Results showed that the combined treatment exerted the optimal anti-tumor effect in both tumor-bearing models. Part II first identified, *via* cell viability assay and RNA-seq, that ferroptosis-related genes were enriched after nintedanib treatment. Subsequent experiment, including cell viability rescue with various cell death inhibitor, assessment of lipid peroxidation, MDA, and PTGS2 levels, and transmission electron microscopy (TEM) visualization of ferroptotic features confirmed that nintedanib enhances radiosensitivity by inducing ferroptosis in tumor cells. Part III delved into the underlying mechanism. First, nintedanib treatment was found to reduce SLC7A11 expression and GSH levels in tumor cells. SLC7A11 overexpression and NAC supplementation confirmed that nintedanib induces ferroptosis through inhibiting SLC7A11 mediated GSH synthesis. Subsequent analyses revealed that nintedanib inhibits expression of ATF4, a regulatory protein of SLC7A11, and radiation upregulates ATF4 expression in a subset of tumor cells. Prognostic analysis conducted on datasets of lung cancer and colorectal cancer revealed that low levels of ATF4 were correlated with better prognosis. Knockdown and overexpession of ATF4 in tumor cells further confirmed that nintedanib enhances ferroptosis sensitivity of tumor cells by suppressing ATF4/SLC7A11/GSH synthesis. Part IV found that combined nintedanib and radiation further upregulated PD-L1 expression in tumor cells. *In vivo* experiments demonstrated that nintedanib combined with radiotherapy increases the number and function of tumor-infiltrating T cells and enhances the efficacy of α-PD-L1 therapy. Part V conducted a preliminary biosafety evaluation by monitoring body weight of tumor-bearing mice, H&E staining of major organs, and blood biochemical analyses. Results showed that the combined strategy has no obvious toxic side effects. NDNB, nintedanib; RT, radiation; RILI, radiation-induced lung injury; RIPF, radiation-induced pulmonary fibrosis; DIILD, drug-induced interstitial lung disease; FINs, ferroptosis inducers; IHC, immunohistochemistry; mIF, multiplex immunofluorescence; CCK-8, cell counting Kit-8; ROS, reactive oxygen species; MDA, malondialdehyde; qRT-PCR, quantitative real-time PCR; GSH, glutathione; KEGG, Kyoto encyclopedia of genes and genomes; GSEA, gene-set enrichment analysis; Ferr-1, ferrostatin-1; Z-VAD, Z-VAD-FMK; Nec-1s, necrostatine-1s; NAC, N-acetyl cysteine; ALT, alanine aminotransferase; AST, aspartate aminotransferase; BUN, blood urea nitrogen; CRE, creatinine; ICD, immunogenic cell death; DAMPs, damage-associated molecular patterns.

nintedanib was combined with immunotherapy[26,27]. However, there is limited clinical and preclinical evidence regarding the combined use of nintedanib and RT.

As a multi-target tyrosine kinase inhibitor targeting PDGFRs, VEGFRs, FGFRs, RET, and Src, nintedanib has been shown to sustain receptor blockade, promote tumor vascular normalization, reduce tumor burden, and improve the tumor immune microenvironment[28-31]. In addition to modifying the tumor microenvironment, nintedanib has been reported to induce tumor cell death and activate endoplasmic reticulum stress in fibroblasts[32,33]. Recent research involving cell death mechanisms indicated that many ferroptosis inducers (FINs)

also trigger endoplasmic reticulum stress signals[34]. Thus, nintedanib may synergize with RT to enhance tumor cell death. While combining nintedanib with RT is an option, the efficacy of the combination requires further validation.

A series of *in vivo* and *in vitro* experiments were performed to determine the efficacy and mechanism underlying the nintedanib and RT antitumor effect, providing a new combination strategy to improve the efficacy of RT (**Study flowchart**).

# Materials and methods

## Cell lines

LLC, MC38, A549, and HCT116 cell lines were sourced from the Oncology Laboratory of Tongji Hospital (Huazhong University of Science and Technology, Wuhan, China). MC38 (murine colon cancer cells) and A549 (human lung cancer cells) were cultured in RPMI-1640 (Hyclone, Logan, UT, USA) and supplemented with 10% fetal bovine serum (160000-044; Gibco, Thermo Fisher Scientific, Inc., Waltham, MA, USA) and 100 U/mL penicillin/streptomycin (15140122; Gibco, Thermo Fisher Scientific, Inc.) and maintained at 37°C in 5% $CO_2$. LLC (murine lung cancer cells) and HCT116 (human colon cancer cells) were cultured in Dulbecco's modified Eagle's medium (Hyclone) with 10% fetal bovine serum and 100 U/mL penicillin/streptomycin under the same conditions.

## Reagents

Nintedanib was purchased from Selleck Chemicals (S1010; Houston, TX, USA). InVivoMab anti-mouse PD-L1 antibody was obtained from BioXcell (clone 10F.9G2, catalog #BE0101; West Lebanon, NH, USA). Z-VAD-FMK (S7023), ferrostatin-1 (S7243), necrostatin-1 (S8037) were purchased from Selleck Chemicals. N-acetyl cysteine (HY-B0215; Monmouth Junction, NJ, USA) was purchased from MCE.

## Experimental animals

A total of 84 C57BL/6 mice and 84 immunocompromised (nude) mice were provided by Jiangsu GemPharmatech Co., Ltd. (Nanjing, China). Male mice were used to establish the LLC tumor-bearing mouse model and female mice were used to establish the MC38 tumor-bearing mouse model[35,36]. MC38 and LLC cells ($1 \times 10^6$) were subcutaneously implanted into syngeneic C57BL/6 and nude mice. MC38 cells transfected with an empty vector or ATF4 plasmids were similarly implanted into nude mice. Mice were randomly assigned to four treatment groups [PBS, nintedanib (50 mg/kg, 5 days on, 1 day off, administered 10 times), RT (8 Gy), anti-PD-L1 antibody (10 mg/kg, once every 3 days, administered 3 times)] when tumor volumes reached 70–100 $mm^3$. The tumor volume was measured using a digital caliper and calculated as $V = [\text{length} \times \text{width}^2] \times 0.5$, where length represents the maximum diameter and width is the shortest diameter. Tumor growth and survival curves were generated from independent experiments. The mice were euthanized by $CO_2$ inhalation as a humane endpoint when the tumor volume reached 2,000 $mm^3$. Death was confirmed by cessation of both respiratory and cardiac activity. Animal experiments were performed under standard laboratory conditions at the Tongji Hospital Laboratory Animal Center with approval from the Ethics Committee of Huazhong University of Science and Technology (Approval No. TJH-202206052).

## RT

*In vitro* and *in vivo* experiments were performed using an X-ray irradiator (RS 2000 Biological System irradiator; Rad Source Technologies Inc., Boca Raton, FL, USA). Tumor-bearing mice were anesthetized by intraperitoneal (i.p.) injection of 1.5% pentobarbital sodium at a dose of 50 mg/kg body weight and received a single X-ray dose fraction (8 Gy) to the area of the subcutaneous tumor using the RS 2000 Biological System irradiator. A heating pad was used during anesthesia until the mice were fully awake. Tumor cells were irradiated at a dose ranging from 2–8 Gy.

## *In vivo* optical imaging analysis

Mice were injected with D-fluorescein i.p. (115144-35-9; GoldBio, St. Louis, Missouri, USA) and anesthetized by i.p. injection of 1.5% pentobarbital sodium at a dose of 50 mg/kg body weight. A heating pad was used during anesthesia until the mice were fully awake. Bioluminescence was detected using an IVIS 200 Xenogen system (IVIS Spectrum; Perkin Elmer, Waltham, MA, USA).

## Histologic analysis and immunohistochemistry (IHC)

Isolated tumors were fixed in 4% paraformaldehyde at 25°C for 48 h, dehydrated, embedded in paraffin wax, and cut into slices for further experiments. The slices were dewaxed,

rehydrated, and underwent antigen repair. Antigen repair was performed using Tris-EDTA buffer [pH 9.0] (Servicebio, Wuhan, China) in a microwave oven at 95°C for 20 min. Next, the slices were blocked with 5% bovine serum albumin (ST023; Beyotime, Shanghai, China) for 30 min at room temperature, then incubated with primary antibodies overnight at 4°C. Primary antibodies used in the experiments included anti-CD3 (1:200, ab16669; Abcam, Cambridge, UK), anti-CD8α (1:2,000, ab217344; Abcam), and anti-Ki-67 (1:200, ab16667; Abcam). After incubation with secondary antibody (1:5,000; Aspen, Wuhan, Hubei, China), the slices were stained using 3,3′-diaminobenzidine (Aspen) and counter-stained using hematoxylin (Aspen). All slices were viewed and imaged under a microscope (Leica, Wetzlar, Germany) and the positive cells were quantified by two blinded pathologists.

## TUNEL assay

Isolated tumors were fixed in 4% paraformaldehyde at 25°C for 48 h, dehydrated, embedded in paraffin wax, and cut into slices for further experiments. The slices were stained using a TUNEL assay kit (11684795910; Roche, Mannheim, Germany) following the manufacturer's protocol. The images were captured using a microscope (Pannoramic MIDI; 3D Histech, Budapest, Hungary) and analyzed using ImageJ software.

## Multiplex immunofluorescence (mIF)

Isolated tumors were fixed in 4% paraformaldehyde at 25°C for 48 h, dehydrated, embedded in paraffin wax, and cut into slices for further experiments. The slices were dewaxed, rehydrated, and underwent antigen repair. Antigen repair was performed using Tris-EDTA buffer [pH 9.0] (Servicebio) in a microwave oven at 95°C for 20 min. The slices were blocked with 5% bovine serum albumin (ST023; Beyotime) for 30 min at room temperature after permeabilization with 0.3% Triton X-100 in PBS for 10 min, then incubated with the following primary antibodies: anti-CD4 (1:2,000, ab183685; Abcam); anti-CD8α (1:2,000, ab217344; Abcam); CD31 (1:500, ab182981; Abcam); and α-SMA (1:100, AF1032; Affinity, Melbourne, AUS). After incubation with fluorescent secondary antibody and DAPI (Servicebio), the immunofluorescence images were captured using a Pannoramic MIDI and analyzed using ImageJ software.

## Apoptosis analysis

Cultured cells ($1 \times 10^5$ cells per sample) were harvested after different treatments. An FITC Annexin V Apoptosis Detection Kit I (556547; BD Pharmingen, San Diego, California, USA) was used to detect cell apoptotic status. Flow cytometric analysis was performed using CytoFLEX LX (Beckman, Brea, CA, USA). The data were analyzed using FlowJo software (v10; BD Biosciences, San Diego, California, USA).

## Colony-forming assay

Cells were seeded at a low density (200–800 cells/well) in 6-well plates and the treatment (drug or radiation) was applied the following day. After 2 weeks of culture the colonies were fixed with 4% buffered paraformaldehyde and stained with 0.01% crystal violet. Colonies containing ≥50 cells were counted and used for statistical analysis.

## Cell counting Kit-8 (CCK-8) assay

Cells from different cell lines were seeded into 96-well plates ($4–7 \times 10^3$ cells per well) and incubated at 37°C in a $CO_2$ incubator for 24 h. Following treatment, the cells were cultured for specific time periods. Cell viability was assessed using the Cell Counting Kit-8 (HY-K0301; MedChem Express, New Jersey, USA) with absorbance measured at 450 nm using a microplate reader (BioTek, Winooski, VT, USA).

## RNA-seq assay

Total RNA from MC38 cell lines was extracted using Trizol (9766; Takara Bio, Shiga, Japan) and purified for library preparation and sequencing on the Illumina Hiseq platform (San Diego, California, USA). RNA sequencing was performed by Novogene (Beijing, China). Analysis of differential gene expression among the four groups was performed with the DESeq2 R package (version 1.20.0). Statistical significance for differential expression was defined as a $P < 0.05$. The R 'clusterProfiler' package was utilized to conduct Kyoto Encyclopedia of Genes and Genomes (KEGG) pathway analysis on the differentially expressed genes (DEGs). The corresponding datasets have been submitted to a public database (Gene Expression Omnibus under the GSE297011 dataset; www.ncbi.nlm.nih.gov/geo).

## Reactive oxygen species (ROS) detection

An ROS Assay Kit (S0034S; Beyotime) was used to detect the generation of intracellular ROS. Cells ($2 \times 10^5$) were seeded in 6-well plates and treated as specified. After co-incubation with 2′,7′-dichlorodihydrofluorescein diacetate (DCFH-DA) for 30 min at 37°C, cells were thrice-washed with cold PBS. The immunofluorescence images were observed using a Pannoramic MIDI and fluorescence intensity was measured using ImageJ.

## Lipid peroxidation measurement

Cells ($2 \times 10^5$) were seeded in 6-well plates and treated as specified. Cultured cells ($3 \times 10^5$ cells per sample) were harvested and stained for 30 min at 37°C with 5 μM BODIPY 581/591 C11 dye (D3861; Invitrogen, Thermo Fisher Scientific, Inc., Waltham, MA, USA) to assess lipid peroxidation. After washing three times with cold PBS, flow cytometric analysis was performed using the CytoFLEX LX. Data were analyzed with FlowJo software (v10).

## Malondialdehyde (MDA) measurement

The MDA content in tumor cells was measured using the corresponding kits (A003-1-2; Nanjing Jiancheng Bioengineering Institute, Nanjing, China) according to the manufacturer's instructions.

## Quantitative real-time PCR (qRT-PCR)

Cells ($5 \times 10^5$) were seeded on 6-well plates and treated as specified. Total RNA was extracted using Trizol and reverse-transcribed to cDNA using the PrimeScript 1st Strand cDNA Synthesis Kit (6110A; Takara Bio). RT-qPCR was performed using ChamQ Universal SYBR qPCR Master Mix (Q711-02; Vanzyme, Nanjing, China) on the ABI-7900HT Sequence Quantification System (Applied Biosystems, Foster, CA, USA), according to the manufacturer's protocol. mRNA expression of the target genes were normalized to β-actin expression and analyzed using the $2^{-\Delta\Delta Cq}$ method. The primer sequences are listed in **Table S1**.

## Transmission electron microscope

Cells were collected after treatment and fixed in 2.5% glutaraldehyde overnight followed by fixation in 1% osmium tetroxide. The cells were stained with 2% uranyl acetate, dehydrated, embedded, and sectioned. Images of the cells were captured using a transmission electron microscope [TEM] (HT7700; Hitachi, Tokyo, Japan).

## Western blot

Total protein was extracted using RIPA buffer (Beyotime) containing 1% phenylmethylsulfonyl fluoride and 1% phosphatase inhibitor (Servicebio). The protein concentration was determined using the Bradford method. Thirty micrograms of protein sample were separated using 8%–10% sodium dodecyl sulfate-polyacrylamide gel electrophoresis and transferred to 0.45 μm polyvinylidene fluoride membrane (Millipore, Billerica, MA, USA, USA). The membrane was probed with primary antibodies overnight at 4°C after incubation with 5% bovine serum albumin for 1 h at room temperature. The membranes were visualized by SuperSignal West Pico Chemiluminescent Substrate (Thermo Scientific) after the membranes were incubated with secondary antibodies (Promoter, Wuhan, China). The signal from the blots was detected using the G:BOX Chemi X system (Syngene, Cambridge, UK) and analyzed using ImageJ software. Western blotting was performed using the following antibodies: GAPDH (1:20,000, 60004-1-lg; Proteintech, Wuhan, China); β-actin (1:5,000, 60008-1-lg; Proteintech); SLC7A11/xCT (1:1,000, A2413; ABclonal, Wuhan, China); γ-H2AX (1:1,000, #9718; Cell Signaling Technology, Danvers, Massachusetts, USA); ATF4 (1:1,000, A18687; ABclonal); ATF3 (1:1,000, #18665; Cell Signaling Technology); NRF2 (1:1,000, #12721, Cell Signaling Technology); P53 (1:1,000, #2524; Cell Signaling Technology).

## Reduced glutathione (GSH) measurement

GSH content in tumor cells was quantified using the corresponding kits (A005-1-2; Nanjing Jiancheng Bioengineering Institute, China) following the manufacturer's protocol.

## Cell transfection

Lentivirus particles targeting human ATF4 (shATF4) were purchased from GeneChem (Shanghai, China), with target sequences as follows: sh1 (-CCACTCCAGATCATTCCTTTA-); sh2 (-GTTGGTCAGTCCCTCCAACAA-); and sh3 (-GCCTAGGTCTCTTAGATGATT-). Viral particles and polybrene (6 μg/mL; GeneChem) were mixed with the cell culture

medium and incubated for 6 h, after which fresh medium was added. Puromycin (2 μg/mL; GeneChem) was used to screen cells with successful transfection. Plasmids containing *SLC7A11* or *ATF4* cDNA were utilized to generate stable SLC7A11 overexpressing human cells, ATF4 overexpressing human cells, and ATF4 overexpressing mouse cells. Transfection was performed using Lipofectamine 3000 (L3000015; Invitrogen, Waltham, MA, USA). pCDH-pCDH-CMV-MCS-ATF4 lentivirus particles were produced by co-transfecting pCDH-pCDH-CMV-MCS-ATF4 with packaging plasmids (pMD2 and pAX2) into HEK293T cells. MC38 cells were infected with pCDH-pCDH-CMV-MCS-ATF4 lentivirus particles and selected with puromycin (2 μg/mL; GeneChem) to establish a stable ATF4-overexpressing MC38 cell line. Western blot analysis confirmed the efficiency of gene knockdown or overexpression.

## Flow cytometry

Cultured cells ($1 \times 10^5$ cells per sample) were harvested and stained with antibodies against PD-L1 (PE anti-mouse CD274, 1:100, clone 10F.9G2, catalog 124307; BioLgend, San Diego, California, USA) at 4°C for 30 min. Tumor tissues were minced and digested with type IV collagenase, hyaluronidase, and DNase (Biosharp, Anhui, China) at 37°C for 1 h, then filtered through 100-μm nylon cell strainers (Biosharp). Lymphocytes were collected, and live/dead staining was performed using eBioscience Fixable Viability Dye eFluor™ 780 (65-0865-14, 1:1,000; Invitrogen). The cell surface was stained with antibodies against CD45 (BV480 anti-mouse CD45, 1:100, clone 30-F11, catalog 566095; BD Horizon, San Diego, California, USA), CD3 (PE anti-mouse CD3, 1:100, clone 17A2, catalog 100205; BioLgend), and CD8a (APC anti-mouse CD8a, 1:100, clone 53-6.7, catalog 100711; BioLgend). The eBioscience FOXP3/Transcription Factor Staining Buffer Set (00-5523-00; Invitrogen) was used before intracellular staining with antibody against Ki-67 (PE/cyanine anti-mouse KI-67, 1:100, clone 16A8, catalog 652425; BioLgend). Flow cytometry was performed using CytoFLEX LX and the data were analyzed using FlowJo software (v10).

## Safety evaluation

The main organs (heart, liver, lungs, colon, spleen, and kidneys) with serum were collected for further analysis at the end of the animal experiments. Organs were sectioned and stained with H&E for histopathologic evaluation of tissue damage. Mouse serum was collected for blood biochemistry analysis, including measurements of alanine aminotransferase (ALT), aspartate aminotransferase (AST), blood urea nitrogen (BUN), and creatinine (CRE), and analyzed using a Chemray 240 Automatic Biochemical Analyzer (Rayto Science, Shenzhen, China).

## Statistical analysis

Statistical analyses were performed using GraphPad Prism 8.0 (San Diego, CA, USA). Data are presented as the mean ± SD unless specified. Repeated-measures ANOVA with Tukey's multiple comparison test were used for animal experiments. Mouse survival curves were calculated using the Kaplan–Meier method and compared by the log-rank test. One- or two-way ANOVA was used for comparisons, as appropriate. A $P$ value < 0.05 was considered statistically significant, with significance noted as $^*P < 0.05$, $^{**}P < 0.01$, $^{***}P < 0.001$, and $^{****}P < 0.0001$.

# Results

## Nintedanib combined with RT significantly inhibits tumor growth *in vivo*

LLC and MC38 cell lines were used to establish tumor models in C57BL/6 mice to evaluate the antitumor efficacy of nintedanib in combination with RT (**Figure 1A**). The *in vivo* antitumor efficacy and safety of nintedanib was assessed in preliminary experiments in MC38 tumor-bearing mice using dose gradients of 30, 50, and 70 mg/kg. The 50 mg/kg dose gradient provided antitumor effects comparable to the antitumor effects achieved with 70 mg/kg. However, the 70 mg/kg regimen resulted in severe diarrhea and weight loss in tumor-bearing mice. Given the robust antitumor effects demonstrated with 2-week 50 mg/kg nintedanib administration in studies by Kutluk Cenik et al., Awasthi et al., and our own research[26,30,37] and to minimize the inevitable esophageal damage caused by gavage administration in mice, the administration frequency of nintedanib was determined to be 50 mg/kg, 5 days on, 1 day off, administered 10 times.

The tumor growth curves of C57BL/6 tumor-bearing mice indicated that the strategy of combining nintedanib with RT had significantly superior anti-tumor efficacy compared to monotherapy (**Figures 1B, C and S1A, B**). Moreover, the combination groups showed the best overall survival compared to other treatment groups and the control group (**Figure 1D, E**). *In vivo* optical imaging of MC38 tumors on days 15 and 30 post-treatment showed that all groups, except the combination

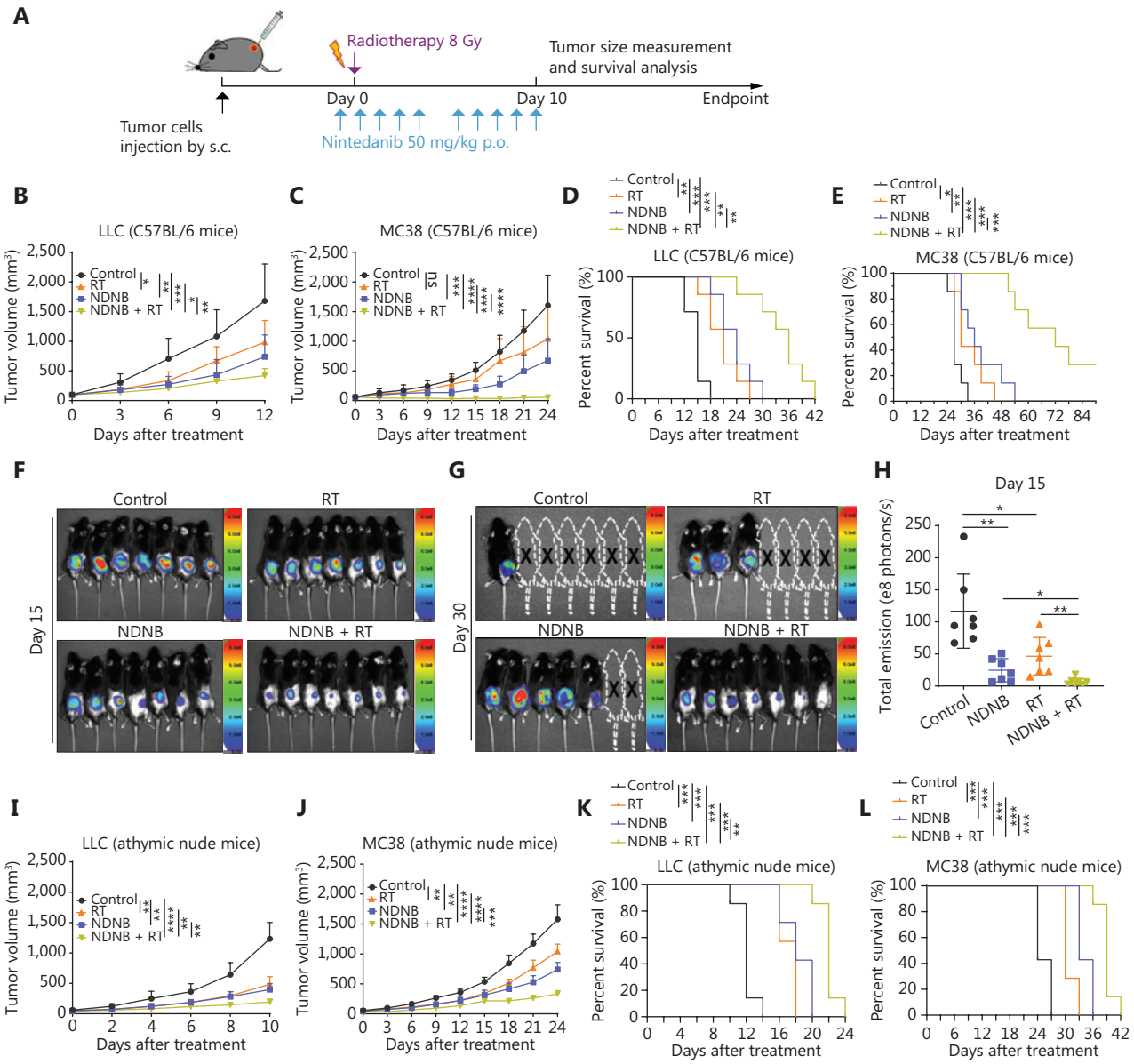


**Figure 1** Antitumor effect of nintedanib combined with radiotherapy *in vivo*. (A) Treatment schedule of tumor-bearing mice. LLC and MC38 cells were implanted subcutaneously into C57BL/6 mice ($n$ = 7 per group). (B, C) Tumor growth curves of tumor-bearing mice. (D, E) Survival curves of tumor-bearing mice. (F, G) *In vivo* fluorescence imaging of MC38 tumor-bearing mice on days 15 and 30 after different treatments. (H) Quantitative analysis of *in vivo* fluorescence imaging of MC38 tumor-bearing mice on day 15 after different treatments. LLC and MC38 cells were implanted subcutaneously into immunocompromised (nude) mice ($n$ = 7 per group). (I–L) Tumor growth and survival curves of LLC and MC38 immunocompromised (nude) tumor-bearing mice. *$P$ < 0.05, **$P$ < 0.01, ***$P$ < 0.001, ****$P$ < 0.0001.

group, had reached the endpoint (**Figure 1F, G**). Fluorescence imaging on day 15 and quantitative analysis further confirmed the antitumor efficacy of nintedanib combined with RT (**Figure 1H**). In addition, immunohistochemical staining for CD3 and CD8 revealed the highest infiltration of immune cells in the tumor periphery and center in the combination group (**Figure S2A–F**). Multiplex immunofluorescence staining also demonstrated an increased ratio of $CD8^+$ T cells-to-$CD4^+$ T cells within the tumor tissues (**Figure S2G, H**). Ki-67 and TUNEL staining were performed to assess cell proliferation

and apoptosis in tumor tissues. As expected, Ki-67, a marker of cell proliferation, was reduced in the treatment groups, with the lowest expression observed in the combination group (**Figure S2I, J**). TUNEL, an indicator of apoptosis, also showed the most prominent efficacy in the combination group (**Figure S2K, L**). These results indicated that nintedanib combined with RT significantly increased the infiltration of immune cells in tumor tissues and had excellent antitumor effect.

Studies have demonstrated that nintedanib increase T cell and DC infiltration, inhibit cancer-associated fibroblast, and enhance immunotherapy efficacy in mice[26,27,38]. LLC and MC38 tumor models were established in athymic nude mice to determine whether the antitumor effects of nintedanib depend on an intact immune system. Tumor growth in nude mice were significantly reduced in the three treatment groups with the combination treatment showing the most effective antitumor response as shown in **Figure 1I–1L**. The strategy of combining nintedanib with RT exerted the optimal antitumor effect in the C57BL/6 and nude mouse tumor-bearing models and the antitumor effect was more pronounced in C57BL/6 tumor-bearing mice with an intact immune system by comparing the survival (**Figure 1D,1E, 1K, and 1L**) and individual tumor growth curves (**Figure S1**) of different tumor-bearing mouse models. Furthermore, the changes in tumor growth between intact and nude tumor-bearing mice were compared at different time points. Immunocompetent tumor-bearing mice model responded more significantly to combination therapy than nude mice (**Figure S2M**), suggesting that the adaptive antitumor immunity is one of the important mechanisms underlying the combination of nintedanib and RT. Although an intact immune system extended tumor-bearing mice survival, the antitumor advantage of the combination treatment was still observed in immunocompromised mice, suggesting that combination treatment remains effective in the absence of an adaptive immune response. These results suggest that nintedanib has the potential to directly act on tumor cells in addition to improving the tumor immune microenvironment, thereby enhancing the anti-tumor efficacy of RT.

## Nintedanib combined with RT significantly suppresses cell proliferation *in vitro*

To investigate the combined therapeutic potential of nintedanib, a series of *in vitro* experiments were performed to evaluate antitumor effects in combination with RT. The results from colony formation and CCK8 assays showed that the combination of nintedanib and radiation significantly inhibited tumor cell proliferation (**Figure S3A, B**). An unbiased RNA-seq analysis was performed to assess changes in gene expression induced by nintedanib and to elucidate the mechanisms underlying the antitumor effects following combination treatment. A heat map of gene expression revealed that nintedanib significantly enhanced the transcriptional changes induced by radiation (**Figure S3C**). Tumor-related KEGG enrichment pathways between the combined and radiation groups and between the nintedanib and control groups were compared to determine the effect of nintedanib on the proliferation and death of tumor cells, which showed significant differences in the expression of genes related to ferroptosis (**Figure S3D, E**). Ferroptosis is an iron-dependent, non-apoptotic form of regulated cell death caused by lipid peroxidation, which is controlled by integrated oxidation and antioxidant systems. Several metabolic pathways, particularly those involving iron, lipids, and amino acids, orchestrate the complex ferroptotic response through direct or indirect regulation of iron accumulation or lipid peroxidation[39]. Gene Set Enrichment Analysis (GSEA) showed that nintedanib impacted the expression of genes related to lipid metabolism, GSH, and amino acid transport in tumor cells (**Figure S3F–H**), indicating that nintedanib may modulate ferroptosis sensitivity and affect key metabolic pathways.

## Nintedanib enhances radio-sensitivity by inducing ferroptosis in tumor cells

The effects of the ferroptosis inhibitor, ferrostatin-1 (Ferr-1), the apoptosis inhibitor, Z-VAD-FMK (Z-VAD), and the necroptosis inhibitor, necrostatin-1s (Nec-1s), were evaluated in tumor cells treated with nintedanib to determine whether nintedanib induces ferroptosis in tumor cells. Various cell death inhibitors could reverse the proportion of late-stage apoptosis (Annexin V+/PI+) induced by nintedanib with ferroptosis inhibitors exhibiting the most significant reversal effect (**Figure 2A**). CCK8 and colony formation assays revealed that ferrostatin-1 more effectively restored cell survival compared to Z-VAD-FMK and necrostatin-1s across multiple tumor cell lines (**Figure 2B, C**). Treatment with ferrostatin-1 increased cell viability in tumor cell lines upon exposure to various concentrations of nintedanib. The

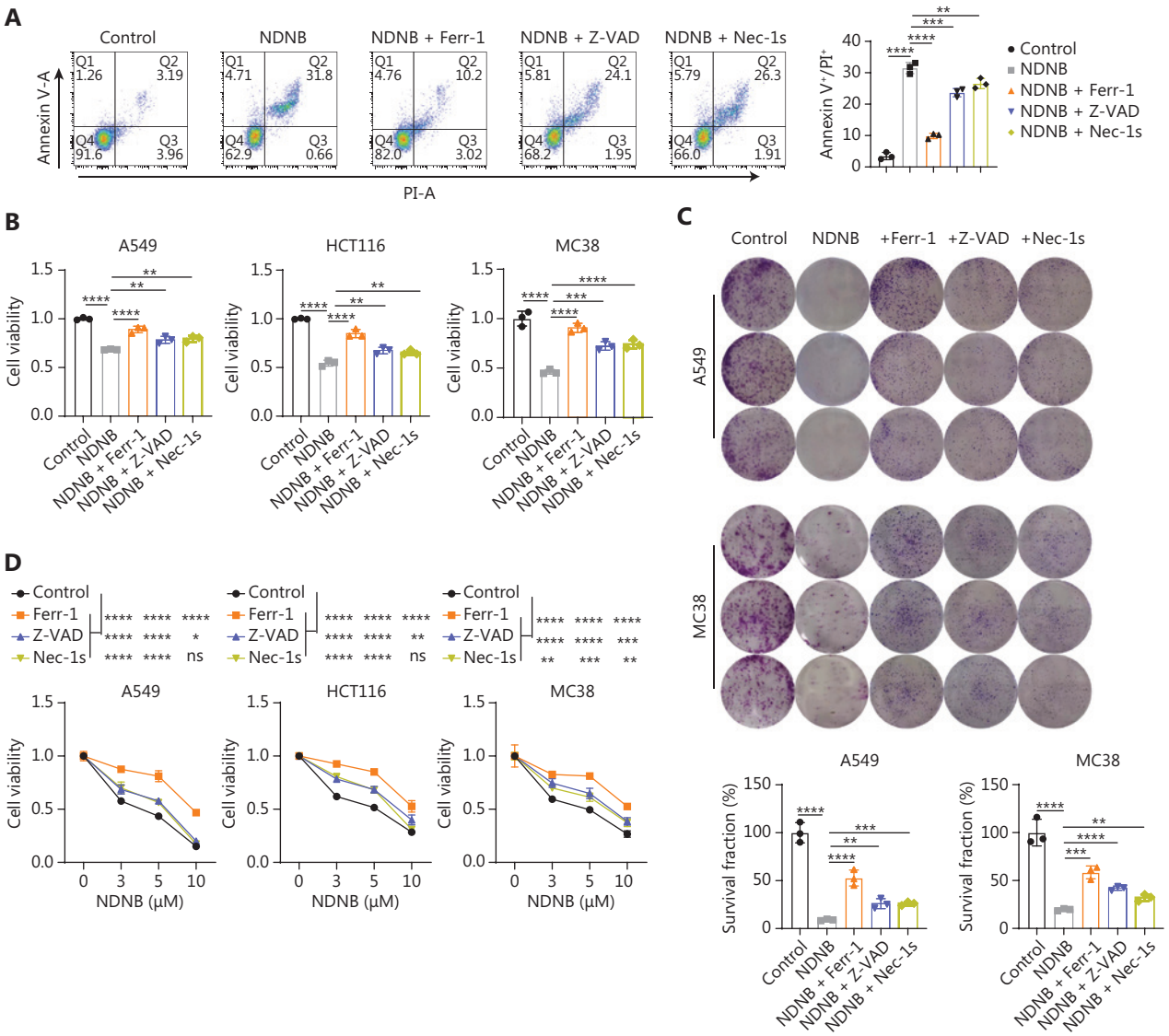


**Figure 2** Continued

restoration of cell survival by Z-VAD-FMK and necrostatin-1s was weaker than ferrostatin-1 in three cell lines (**Figure 2D**). These results suggested that ferroptosis is partially responsible for the efficacy of nintedanib.

Ferroptosis-induced cytotoxicity relies on the production of ROS[40,41]. Nintedanib was shown to promote ROS production in tumor cells (**Figure 2E**). Given that lipid peroxidation is a hallmark of ferroptosis, BODIPY™ 581/591C11 staining was used to assess lipid peroxidation levels. Nintedanib significantly induced lipid peroxidation in tumor cells (**Figure 2F**). Moreover, MDA, a major byproduct of lipid peroxidation, was also elevated following nintedanib treatment (**Figure 2G**). Furthermore, the mRNA levels of PTGS2, a key genetic marker of ferroptosis, were upregulated in tumor cells following nintedanib treatment (**Figure 2H**).

In addition, nintedanib demonstrated a synergistic effect with radiation in promoting ROS production (**Figure 3A**), inducing lipid peroxidation (**Figure 3B**) and increasing MDA (**Figure 3C**) and PTGS2 (**Figure 3D**) levels. TEM revealed significant morphologic alterations in the cellular ultrastructure of tumor cells treated with nintedanib and radiation with the combined treatment showing the most prominent ferroptotic features, including changes in mitochondrial morphology, such as decreased mitochondrial

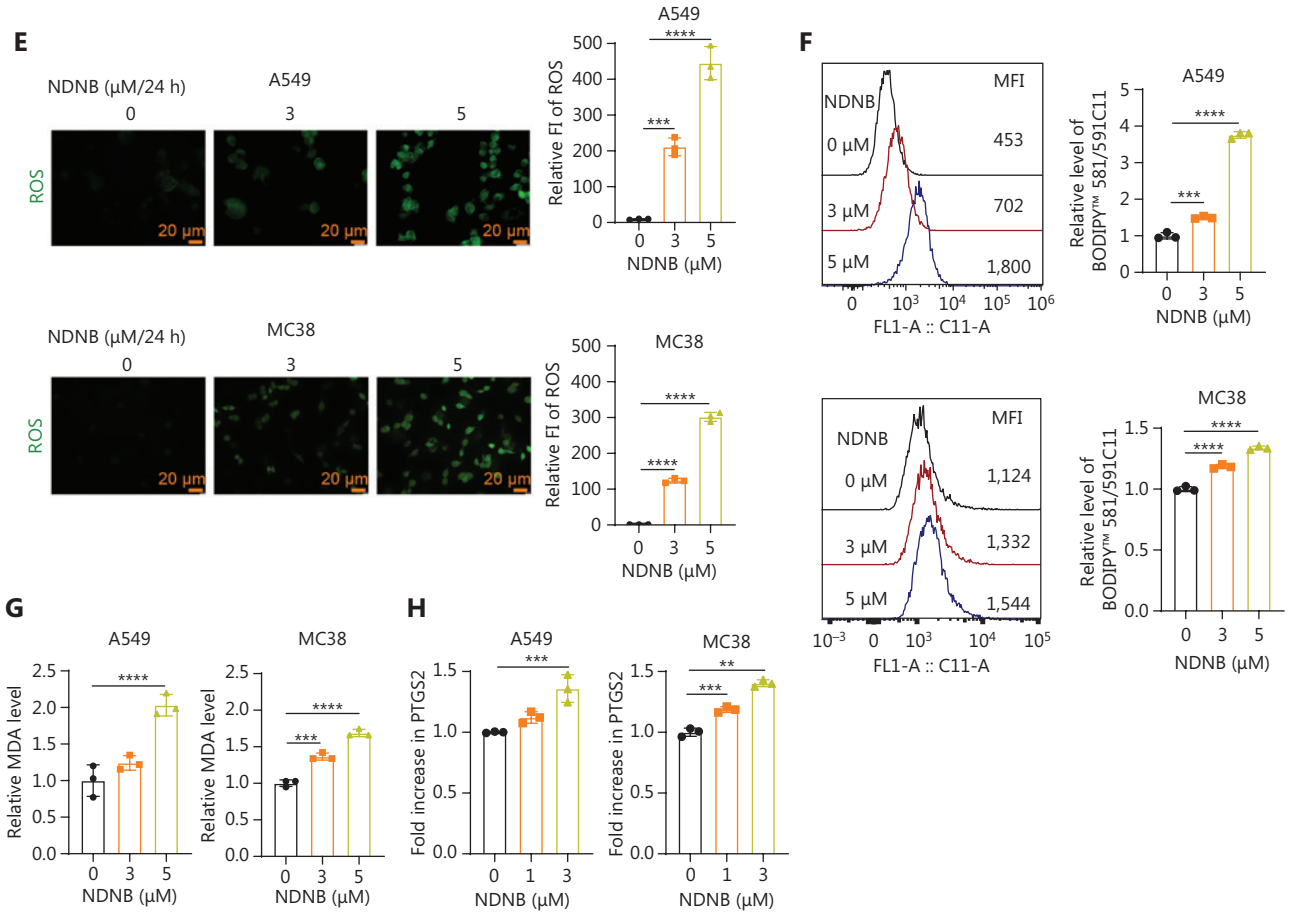


**Figure 2** Nintedanib induces ferroptosis in tumor cells. (A) Representative flow cytometry profiles of annexin V-FITC/PI staining and statistical analysis of MC38 that were pretreated with or without ferrostatin-1 [Ferr-1] (2 μM), carbobenzoxy-valyl-alanyl-aspartyl-[O-methyl]-fluoromethylketone [Z-VAD] (5 μM), and necrostatine-1s [Nec-1s] (2 μM) for 24 h followed by treatment with nintedanib (5 μM) for 24 h. (B) Pretreatment with or without ferrostatin-1 [Ferr-1] (2 μM), carbobenzoxy-valyl-alanyl-aspartyl-[O-methyl]-fluoromethylketone [Z-VAD] (5 μM), and necrostatine-1s [Nec-1s] (2 μM) for 24 h. A549, HCT116, and MC38 cells were treated with nintedanib (5 μM) for 24 h, then cell viability was detected by CCK8. (C) Clonogenic assay for A549 and MC38 cells that were treated with nintedanib (3 μM) in combination with DMSO, ferrostatin-1 (2 μM), Z-VAD (5 μM), or Nec-1s (2 μM), mean ± SD, $n$ = 3. (D) Cell viability for A549, HCT116, and MC38 cells that were pretreated with or without ferrostatin-1 [Ferr-1] (2 μM), carbobenzoxy-valyl-alanyl-aspartyl-[O-methyl]-fluoromethylketone [Z-VAD] (5 μM), and necrostatine-1s [Nec-1s] (2 μM) for 24 h followed by treatment with different dose of nintedanib for 24 h. A549 and MC38 treated with different dose of nintedanib for 24 h. (E) The reactive oxygen species (ROS) level. Scale bar: 20 μm. (F) Lipid peroxidation levels. (G) MDA levels. (H) PTGS2 expression. *$P$ < 0.05, **$P$ < 0.01, ***$P$ < 0.001, ****$P$ < 0.0001.

size, increased membrane density, and reduced or vanished cristae (**Figure 3E**). Western blot analysis showed that an increase in γH2AX induced by radiation was alleviated by 24 h, whereas nintedanib prolonged γH2AX production, a marker of DNA damage, further supporting the notion that nintedanib enhances tumor cell stress (**Figure 3F**). These results suggested that nintedanib enhances radiosensitivity by inducing ferroptosis in tumor cells.

## Nintedanib enhances ferroptosis sensitivity of tumor cells by suppressing SLC7A11-mediated GSH synthesis

Nintedanib significantly suppressed SLC7A11 expression (**Figure 4A**), a key regulator of GSH synthesis and utilization. GSH, an antioxidant, has a critical role in preventing lipid peroxidation and ferroptosis[42]. SLC7A11 expression was reduced

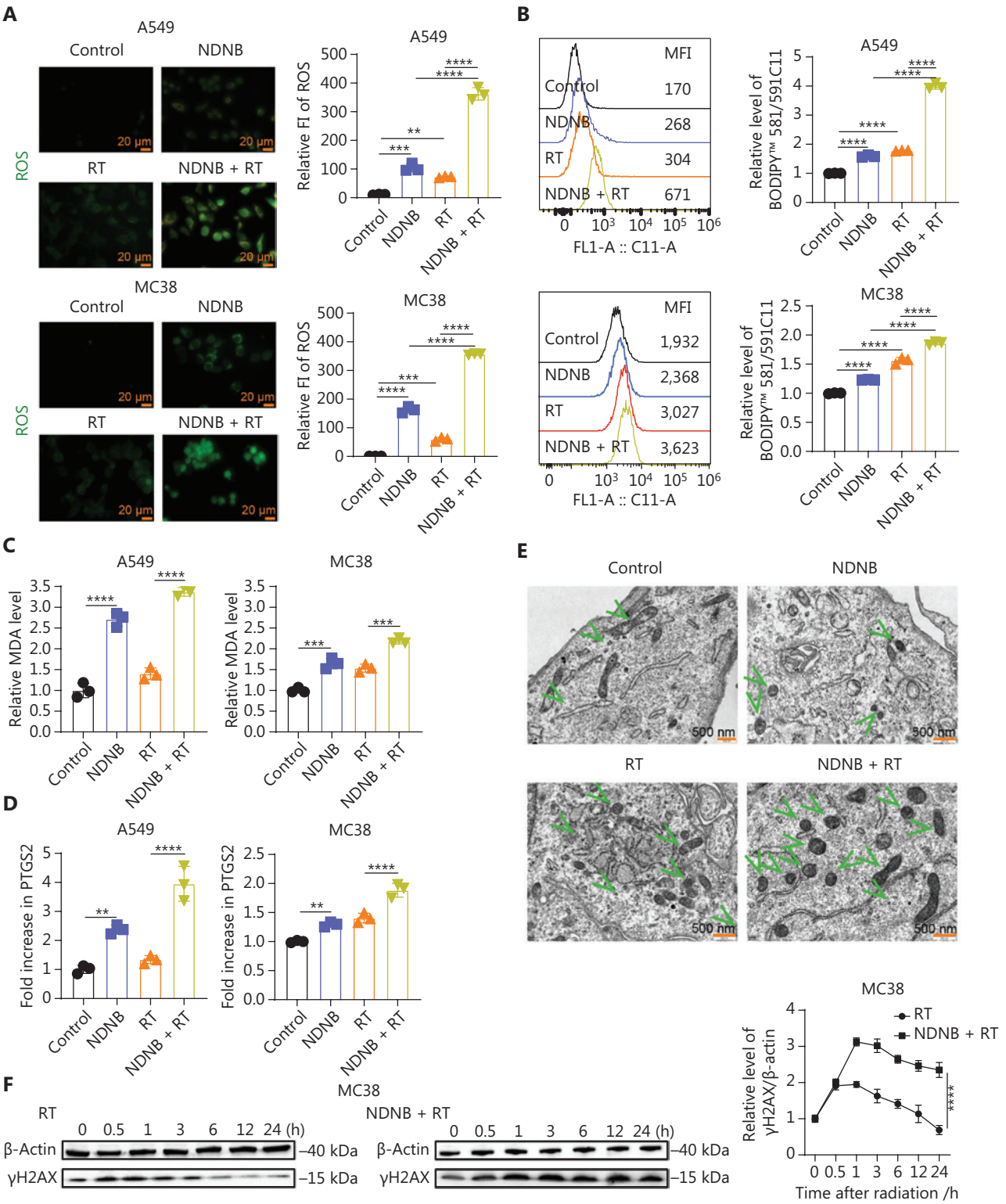


**Figure 3** Nintedanib enhances radiosensitivity by promoting ferroptosis in tumor cells. A549 and MC38 cells treated with nintedanib (3 μM) and radiation (8 Gy) for 24 h. (A) The reactive oxygen species (ROS) level. Scale bar: 20 μm. (B) Lipid peroxidation levels. (C) MDA levels. (D) PTGS2 expression. (E) Transmission electron microscopy imaging results of MC38 in different experimental groups. Arrows indicate mitochondria. Scale bar: 500 nm. (F) The expression and quantitative analysis of γH2AX in MC38 cells was determined by western blotting. *$P$ < 0.05, **$P$ < 0.01, ***$P$ < 0.001, ****$P$ < 0.0001.

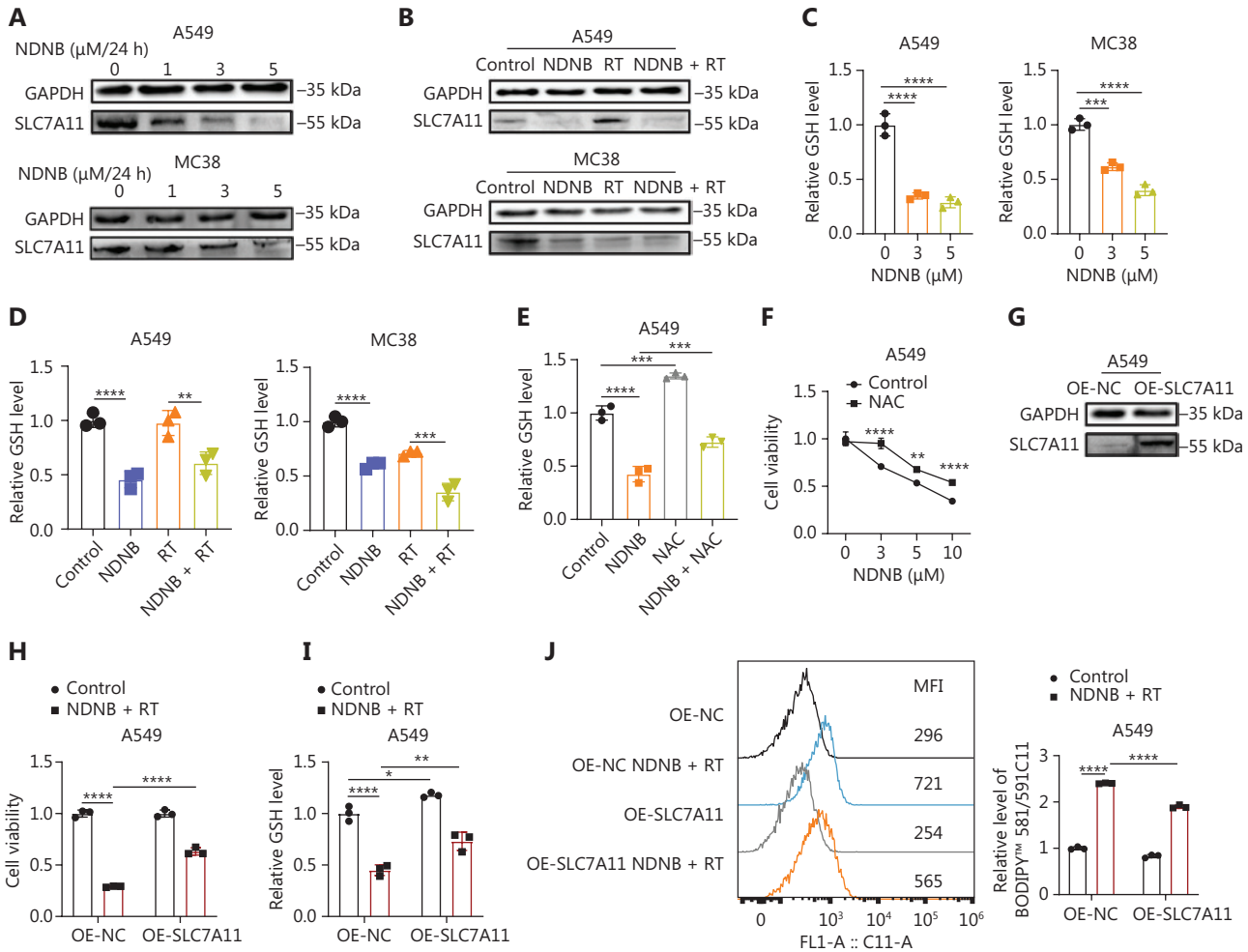


**Figure 4** Nintedanib induces ferroptosis through inhibiting SLC7A11-mediated GSH synthesis. (A, B) The expression and quantitative analysis of GAPDH and SLC7A11 in A549 and MC38 cells was determined by western blotting. (C, D) GSH levels in A549 and MC38 cells after different treatments. (E, F) GSH levels and cell viability for A549 cells that were pretreated with or without N-acetyl cysteine [NAC] (5 mM) for 24 h followed by treatment with nintedanib for 24 h. (G) The expression of SLC7A11 in A549 cells expressing vector control (NC) or SLC7A11 was determined by western blotting. (H–J) Cell viability, GSH levels, and lipid peroxidation levels in NC and OE-SLC7A11 A549 cells after different treatments. *$P$ < 0.05, **$P$ < 0.01, ***$P$ < 0.001, ****$P$ < 0.0001.

by radiation in the MC38 cell line, while SLC7A11 expression was activated in the A549 cell line (**Figure 4B**). Despite these different responses to radiation, nintedanib consistently inhibited SLC7A11 expression in both cell lines, leading to a reduction in GSH levels (**Figure 4C, D**).

NAC was used to promote GSH production to further explore the relationship between GSH synthesis and nintedanib-induced ferroptosis. NAC significantly enhanced GSH levels in nintedanib-treated and untreated A549 cells (**Figure 4E**) and restored cell viability following nintedanib treatment (**Figure 4F**). In addition, SLC7A11-overexpressing A549 cells were generated to confirm the role of SLC7A11 in nintedanib-induced ferroptosis (**Figure 4G**). Overexpression of SLC7A11 notably reversed the reduction in cell viability (**Figure 4H**), GSH depletion (**Figure 4I**), and lipid peroxidation enhancement (**Figure 4J**) induced by nintedanib and radiation.

These results indicated that nintedanib sensitizes tumor cells to radiation by inhibiting SLC7A11-mediated GSH synthesis.

## ATF4 is involved in nintedanib-induced SLC7A11 downregulation

Previous studies identified stress sensors, including ATF4, NRF2, ATF3, and P53, as regulators of SLC7A11

expression[43-45]. To assess the impact of nintedanib on these regulatory proteins, expression was evaluated following treatment. Western blot analysis revealed that nintedanib significantly inhibited ATF4 expression, while having no effect on other SLC7A11 regulators (**Figure 5A**). Given that ATF4 binds to amino acid response elements to promote SLC7A11 transcription[46-48], it was hypothesized that ATF4 is a crucial target through which nintedanib induces ferroptosis in tumor cells. RNA-seq analysis of downstream genes of ATF4 in nintedanib-treated tumor cells revealed a gene expression profile resembling that of ATF4-deficient hepatocytes (**Figure 5B**), indicating increased sensitivity to ferroptosis[49].

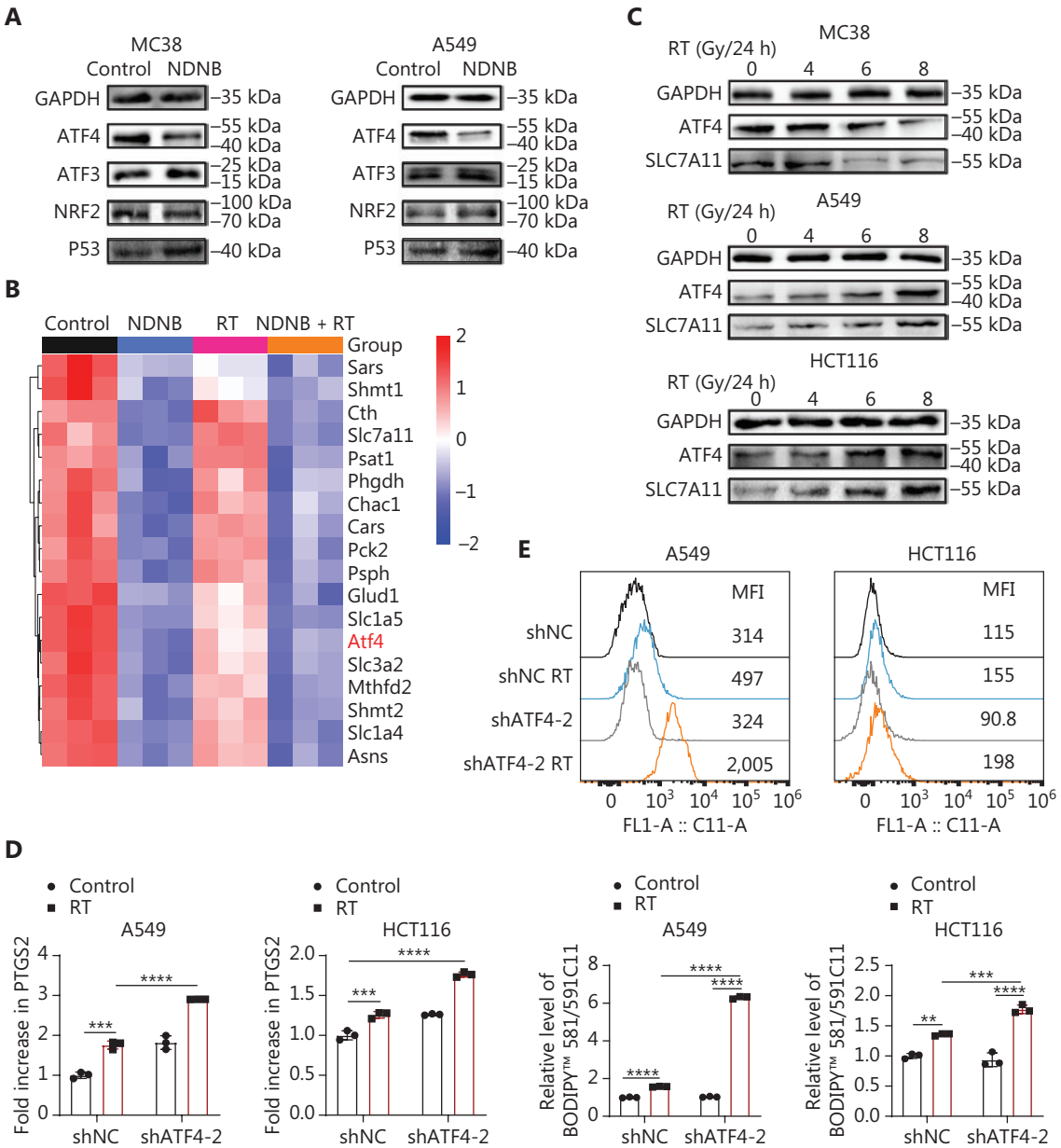


**Figure 5** ATF4 knockdown promoted radiosensitivity of tumor cells. (A) The expression and quantitative analysis of GAPDH, ATF4, ATF3, NRF2, and P53 in A549 and MC38 cells was determined by western blotting. (B) The level of ATF4-related genes in RNA-seq data of MC38 cells. (C) The expression and quantitative analysis of GAPDH, ATF4, and SLC7A11 in MC38, A549, and HCT116 treated with increasing dose of radiation. (D, E) PTGS2 expression and lipid peroxidation level in A549 (shNC and shATF4) and HCT116 (shNC and shATF4) after different treatments for 24 h. *$P$ < 0.05, **$P$ < 0.01, ***$P$ < 0.001, ****$P$ < 0.0001.

This further supports the idea that nintedanib induces ferroptosis by inhibiting ATF4 expression.

In addition, the effect of radiation on ATF4 expression varied among different cell types. Radiation led to downregulation of ATF4/SLC7A11 in the MC38 cell line and upregulation in A549 and HCT116 cells (**Figure 5C**). This finding suggests that ATF4 may contribute to radio-resistance by preventing ferroptosis in tumor cells. To investigate this finding further, ATF4 knockdown and ATF4 overexpression cell lines were created in A549 and HCT116 cells (**Figure S4A and S4C**). Colony formation assays demonstrated that ATF4 has a role in radiation resistance (**Figure S4B and S4D**). Elevated levels of PTGS2 and lipid peroxidation in ATF4 knockdown cells indicated that ATF4 mediates resistance to radiation-induced ferroptosis (**Figure 5D, E**). Furthermore, ATF4 expression was correlated with a poor prognosis in lung cancer (GSE30219, GSE37745, and GSE4573; **Figure S4E**) and colorectal cancer (GSE17538; **Figure S4E**) as revealed by Kaplan–Meier curves (https://kmplot.com). These results suggest the potential of targeting ATF4 to enhance the antitumor efficacy of radiotherapy.

Nintedanib was shown to reverse the radiation-induced upregulation of ATF4 expression in A549 and HCT116 cell lines (**Figure 6A**). ATF4-overexpressing A549 and MC38 cell

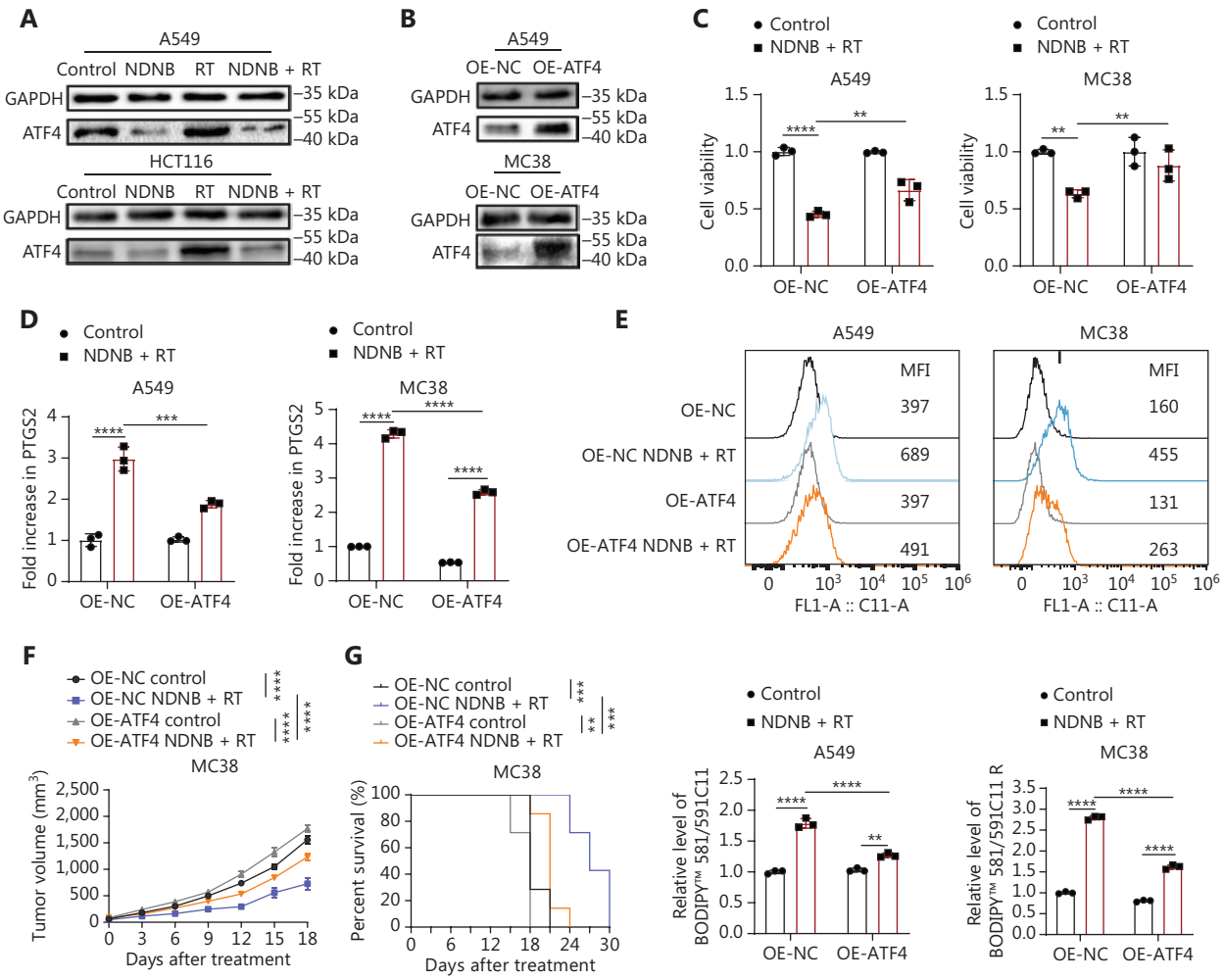


**Figure 6** Nintedanib enhances radiosensitivity of tumor cells by inhibiting ATF4. (A) The expression and quantitative analysis of GAPDH and ATF4 in A549 and HCT116 cells was determined by western blotting. A549 and MC38 cells were transfected with an empty vector or ATF4 plasmids. (B) The expression of GAPDH and ATF4 in A549 and MC38 cells expressing vector control (NC) or ATF4 was determined by western blotting. (C–E) Cell viabilities, PTGS2 expression and lipid peroxidation levels in A549 (NC and OE-ATF4) and MC38 (NC and OE-ATF4) after different treatments for 24 h. MC38 cells (vector control and OE-ATF4) were implanted subcutaneously into C57BL/6 mice ($n$ = 7 per group). (F, G) Tumor growth and survival curves of tumor-bearing mice ($n$ = 7 per group). *$P$ < 0.05, **$P$ < 0.01, ***$P$ < 0.001, ****$P$ < 0.0001.

lines were constructed to confirm the effect of nintedanib on ATF4 (**Figure 6B**). ATF4 overexpression mitigated the reduction in cell viability (**Figure 6C**), the increase in PTGS2 transcription (**Figure 6D**), and the enhancement of lipid peroxidation (**Figure 6E**) caused by nintedanib and radiation. Furthermore, subcutaneous tumor models were established by injecting these cell lines into the flanks of nude mice. Treatment with nintedanib and RT significantly inhibited tumor growth, an effect that was partially reversed by ATF4 overexpression (**Figure 6F, G**).

CD31, an angiogenic biomarker, is commonly used to assess blood vessel density in tumor tissues, while α-SMA$^+$/CD31$^+$ expression reflects tumor vascular perfusion, indicating vascular normalization[50]. Immunofluorescence staining for CD31 and α-SMA was performed on tumor tissues to determine whether the angiogenic effects of nintedanib are linked to ATF4 inhibition. The results (**Figure S5A–C**) demonstrated that the nintedanib anti-angiogenic effect was independent of ATF4 inhibition.

## Nintedanib combined with RT enhances α-PD-L1 therapy efficacy

Recent studies have highlighted that ferroptosis-related lipid peroxides act as identifying signals that promote the recognition and processing of tumor antigens by dendritic cells, activate cytotoxic T lymphocytes, and enhance tumor immunotherapy[51]. In addition, the efficacy of immunotherapy has long been considered to be associated with PD-L1 expression in tumors[52]. Therefore, PD-L1 expression was determined on the surface of tumor cells after nintedanib combined with radiation stimulation. The combined treatment further upregulated PD-L1 in tumors compared to other treatments, indicating the potential of the therapeutic strategy combining nintedanib with RT and anti-PD-L1 therapy, as shown in **Figure 7A**. Next, animal models were used to verify that the triple treatment strategy further inhibited tumor volume growth and prolonged the tumor-bearing survival time of mice compared to the dual treatment strategy (**Figure 7B–E**). Immunohistochemistry was used to determine whether the number of CD8$^+$ cells in the tumor center differed in each group. As demonstrated by the positive cell count analysis, triple therapy group tumors had a greater CD8$^+$ cell infiltrate compared to the other treatment groups (**Figure 7F**). Furthermore, flow cytometry analysis revealed that the proliferation of CD3$^+$ and CD8$^+$ T cells was most robust in the combination treatment group (**Figure 7G–I**). Therefore, nintedanib combined with RT promotes ferroptosis in tumors and enhances the effect of immunotherapy by up-regulating PDL1 in tumors and increasing the number and function of tumor-infiltrating T cells.

## Preliminary biosafety evaluations of combination treatment of nintedanib and RT in a mouse model

Finally, the safety of nintedanib in combination with RT was assessed. Mouse weight monitoring throughout the experiment did not show significant changes (**Figure S6A, B**). Hematoxylin and eosin staining of major organs revealed no pathologic alterations (**Figure S6C**) and routine blood biochemical analyses indicated no significant abnormalities in organ function (**Figure S6D**). No deterioration of the overall health status of mice, significant weight loss, or spontaneous death of the animals was observed during the experiments. These results provide preliminary evidence supporting the efficacy and safety of nintedanib combined with RT in tumor treatment.

# Discussion

Ionizing radiation induces potent ferroptosis, which has a critical role in the anticancer effects of RT[53,54]. Studies have shown that radiation potently induces lipid peroxidation and ferroptosis in cell lines, xenograft tumors, and cancer patients by increasing ROS generation, increasing biosynthesis of polyunsaturated-fatty-acid-containing phospholipids (PUFA-PLs), and reducing GSH synthesis[53,55,56]. Mechanistically, radiation leads to the excessive generation of ROS by initiating the radioactive decomposition of intracellular water, stimulating the activity of oxidase, and altering the structure or function of mitochondria[57]. PUFA-PLs in cellular membranes are particularly prone to peroxidation under conditions of elevated iron or ROS. The toxic accumulation of lipid peroxides in cellular membranes compromises membrane integrity, ultimately leading to ferroptosis[58]. As an important component of the cellular antioxidant system, defects in the SLC7A11/GSH pathway make tumor cells more susceptible to oxidative stress and subsequently lead to ferroptosis[39].

Nintedanib has been shown to have excellent anticancer activity in multiple preclinical and clinical studies in recent years but the specific anticancer mechanism and appropriate

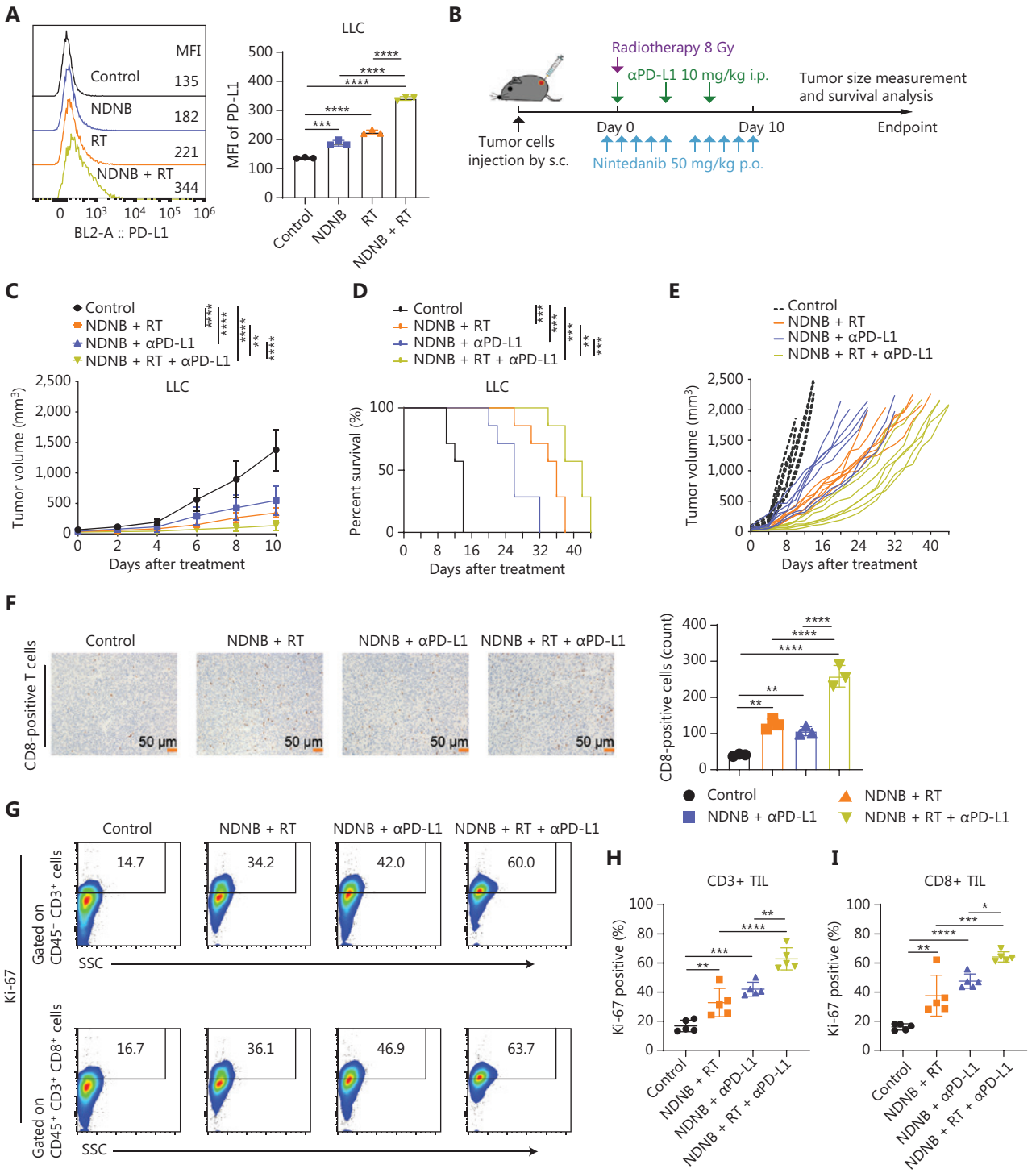


**Figure 7** The antitumor activity of nintedanib combined with radiotherapy and immunotherapy. (A) LLC cells treated with nintedanib (3 μM) and radiation (8 Gy) for 24 h. Surface expression of PD-L1 were determined by flow cytometry. (B) Treatment schedule of tumor-bearing mice. LLC cells were implanted subcutaneously into C57BL/6 mice ($n$ = 7 per group). (C, D) Tumor growth curves and survival curves of LLC tumor-bearing mice. (E) Individual tumor volume curves in LLC tumor survival experiment of C57BL/C mice. (F) Representative images of CD8 IHC staining in LLC tumors and their quantitative analysis. Scale bar: 50 μm. (G–I) Ki-67 in $CD3^+$ T cells and $CD3^+CD8^+$ T cells from TIL of LLC tumors and their quantitative analysis. *$P$ < 0.05, **$P$ < 0.01, ***$P$ < 0.001, ****$P$ < 0.0001.

treatment strategy have not been thoroughly studied. Previous studies have shown that nintedanib inhibits cell proliferation and promotes cell apoptosis by inhibiting ERK, AKT, STAT3, and mTOR[32,59-61]. In this study significant antitumor effects of nintedanib combined with RT were confirmed across a variety of solid tumor models. Downregulation of ATF4 expression, reduced activity of the SLC7A11 system, and subsequent decrease in GSH synthesis were observed following nintedanib treatment, which facilitated lipid peroxidation and ferroptosis in tumor cells. FINs are emerging anticancer agents[62,63] that enhance tumor cell radiosensitivity[64-66]. Nintedanib may act as a potential FIN and exerts a synergistic effect with RT. Notably, nintedanib-induced cell death can also be partially reversed by inhibitors of apoptosis and necroptosis, suggesting that the underlying mechanisms are diverse. Further investigation is needed to explore these mechanisms and the regulatory networks.

ATF4, which is frequently elevated in cancer cells[67], promotes cell survival and tumor growth by controlling the expression of a wide range of adaptive genes that allow cells to endure periods of stress, such as hypoxia or amino acid limitation[68]. We believe the use of ATF4 as a regulatory target provides a promising therapeutic pathway. As one of the main genes regulated by ATF4, SLC7A11 promotes the synthesis of GSH, maintains the REDOX balance of cells, protects cells from oxidative stress damage, and prevents ferroptosis caused by lipid peroxidation[48]. Regulation of the ATF4/SLC7A11 pathway by radiation appears to be background dependent. Radiation-induced upregulation of ATF4 in some tumor cells may act as an adaptive response to protect against ferroptosis, while downregulation of ATF4 in other tumor cells may contribute to radiation-induced ferroptosis. Specifically, radiation induced upregulation of ATF4 expression in A549 and HCT116 cells to resist ferroptosis, which is consistent with a previous study that reported that radiation induces the conversion of polyunsaturated fatty acid phospholipid hydroperoxides (PUFA-PL-OOH) to polyunsaturated fatty acid phospholipid alcohols (PUFA-PL-OH) by upregulating SLC7A11 expression to resist ferroptosis[53]. Radiation and nintedanib synergistically inhibited ATF4 expression in the MC38 cell line, which aligns with the conclusion of another study that radiation induces ferroptosis by activating ATM to inhibit SLC7A11 expression[55]. Despite the different responses of ATF4 expression to radiation in various tumor cell lines, downregulation of ATF4 and SLC7A11 expression, decreased GSH synthesis, and increased lipid peroxidation and radio-sensitivity of tumor cells were observed following nintedanib treatment. Targeting ATF4 for therapeutic purposes offers a promising approach and the ability of nintedanib to inhibit the ATF4/SLC7A11 pathway provides a promising strategy for enhancing the efficacy of RT.

Widjaja et al. reported that nintedanib upregulates the expression of the endoplasmic reticulum stress marker, BIP, in human fibroblasts in a dose-dependent fashion[32], suggesting that inhibition of ATF4 by nintedanib might occur independent of eIF2α regulation. While the precise mechanism by which nintedanib regulates ATF4 expression requires further exploration, several studies provide valuable insights. Previous studies have reported that nintedanib effectively inhibits the mTOR, JAK/STAT3, and TGFβ signaling pathways[33,60,61,69]. mTOR pathway activation and STAT3 phosphorylation have been shown to induce ATF4 expression and the downstream targets in an eIF2α-independent manner[70-72]. In addition, one study demonstrated that TGF-β1-induced ATF4 expression relies on the cooperation between Smad3 signaling and activation of mTORC1 and the downstream target, eukaryotic translation initiation factor, 4E-BP1[73]. Given these findings, nintedanib may regulate ATF4 through the coordinated modulation of multiple signaling pathways.

Furthermore, the intact immune system significantly extended the survival of tumor-bearing mice in the nintedanib combined with RT treatment group. The combination of nintedanib and RT increased the infiltration and function of $CD8^+$ T cells in tumor centers. Additionally, significant antitumor benefits were observed with the triple combination of nintedanib, RT, and immunotherapy in the LLC tumor model, a "cold" tumor, further underscoring the potential of nintedanib as an effective therapeutic agent. Nintedanib promotes tumor vascular normalization, enhances T cell and dendritic cell infiltration, inhibits cancer-associated fibroblasts, and improves the efficacy of immunotherapy in mice[26,27,38]. In addition, ferroptosis in tumor cells contributes to the activation of $CD8^+$ T cells, thereby enhancing the antitumor effects of α-PD1/α-PD-L1[74]. Clinical trials have already established 150 mg of nintedanib twice daily as the recommended dose for combination with pembrolizumab[21]. Ongoing clinical studies are evaluating the combination of nintedanib with immunotherapy across multiple expansion cohorts. Hence, nintedanib induces ferroptosis in tumor cells, while simultaneously enhancing the infiltration and function of tumor-infiltrating T cells. The findings herein provide supporting evidence for the clinical strategy of combining nintedanib with immunotherapy and RT.

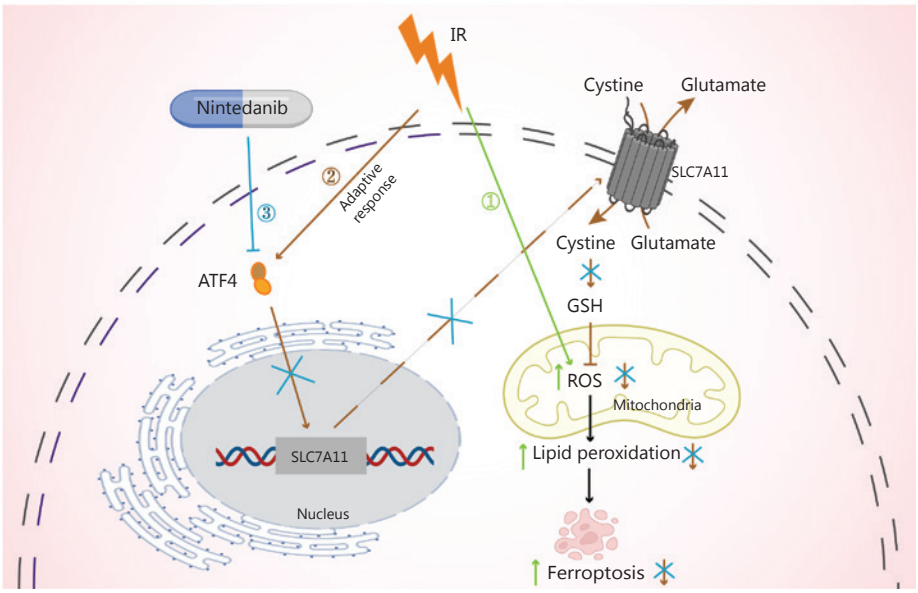


**Figure 8** Schematic model of radio-sensitization by nintedanib through inhibition of the ATF4/SLC7A11/GSH pathway that mediates negative regulation of ferroptosis. SLC7A11 participates in the extracellular uptake of cystine and the release of glutamate, promoting the synthesis of GSH, which is an essential cofactor for cells to eliminate ROS. Excessive accumulation of ROS leads to lipid peroxidation and triggers ferroptosis. In this model, ferroptosis is presumably a balanced effect *via* two counteracting IR-responsive cellular pathways (pathways 1 and 2); nintedanib (pathway 3) however disrupts this balance: (1) Direct IR response (in green): IR induces ROS, which promotes lipid peroxidation and ferroptosis. (2) Adaptive IR response (in brown): IR upregulates ATF4 expression[75,76], which transactivates SLC7A11 expression; this promotes SLC7A11-mediated cystine uptake into cells and GSH synthesis, thereby inhibiting ferroptosis. (3) Nintedanib (in blue), inhibits the ATF4 expression, thereby inhibiting the SLC7A11-dependent negative regulatory pathway of ferroptosis (pathway 2), and subsequently shifting the balance to promote ferroptosis and enhance radiosensitivity.

In summary, this study confirmed the safety and efficacy of nintedanib in combination with RT for the treatment of solid tumors, elucidates the mechanism by which nintedanib enhances radiosensitivity, and introduces a new therapeutic strategy for cancer treatment. However, there were some limitations in this study that could be addressed in future research. As a central protein in cellular stress, ATF4 is involved in a complex signaling network. Further investigation into the regulatory pathways is warranted. Given the extensive use of nintedanib in treating interstitial lung diseases, the effectiveness of nintedanib combined with radiotherapy in an *in situ* lung cancer model with concurrent interstitial lung disease merits further exploration. In addition, further clinical evaluations are necessary to assess the safety and efficacy of nintedanib combined with RT in cancer therapy.

## Conclusions

This study provided a new strategy option for tumor treatments. ATF4 mediates radiation-induced ferroptosis resistance phenotype in tumor cells. Nintedanib induces ferroptosis of tumor cells by inhibiting ATF4/SLC7A11/GSH synthetic system and act as a promising agent combining with RT (**Figure 8**).

## Acknowledgements

We thank the Medical Subcenter of HUST Analytical & Testing Center and Experimental Medicine Center (Tongji Hospital, Tongji Medical College, Huazhong University of Science and Technology) in data acquisition. We thank Bullet Edits Limited for the linguistic editing and proofreading of the manuscript.

## Grant support

This work was supported by State Key Program of National Natural Science Foundation of China (Grant No. 82130092); the General Program of National Natural Science Foundation

of China (Grant No. 82373522), and the National Natural Science Foundation of China (Grant No. 82404196).

## Conflict of interest statement

No potential conflicts of interest are disclosed.

## Author contributions

Conceived and designed the analysis: Chunya Li, Jingyao Tu and Xianglin Yuan.
Collected the data: Chunya Li, Jingyao Tu and Aifeina Aili.
Contributed data or analysis tools: Qingqing Yu, Mu Yang and Qiyuan Feng.
Performed the analysis: Chunya Li, Duo Xu and Bo Liu.
Wrote the paper: Chunya Li, Jingyao Tu and Xianglin Yuan.

## Data availability statement

The data generated in this study are available upon request from the corresponding author.

## References

1. Brown S, Banfill K, Aznar MC, Whitehurst P, Faivre Finn C. The evolving role of radiotherapy in non-small cell lung cancer. Br J Radiol. 2019; 92: 20190524.
2. Delaney G, Jacob S, Featherstone C, Barton M. The role of radiotherapy in cancer treatment: estimating optimal utilization from a review of evidence-based clinical guidelines. Cancer. 2005; 104: 1129-37.
3. Huayamares SG, Loughrey D, Kim H, Dahlman JE, Sorscher EJ. Nucleic acid-based drugs for patients with solid tumours. Nat Rev Clin Oncol. 2024; 21: 407-27.
4. Wang J, Liu F, Wu YY, Zhou L, Hu GY, Yang L. Survival outcomes of patients with cervical esophageal cancer who received definitive radiotherapy: a retrospective study conducted in a single institution. Oncol Transl Med. 2020; 6: 135-42.
5. Lindegaard AM, von Buchwald C, Rasmussen JH, Specht L, Vogelius IR, Zamani M, et al. Outcome in patients with isolated regional recurrence after primary radiotherapy for head and neck cancer. Head Neck. 2020; 42: 3161-70.
6. Ning MS, Ahobila V, Jhingran A, Stecklein SR, Frumovitz M, Schmeler KM, et al. Outcomes and patterns of relapse after definitive radiation therapy for oligometastatic cervical cancer. Gynecol Oncol. 2018; 148: 132-8.
7. Huang L, Chen S, Yang WT, Shao Z. Risk factors of locoregional relapse in locally advanced breast cancer treated with neoadjuvant chemotherapy following mastectomy and radiotherapy. Oncotarget. 2017; 8: 39703-10.
8. Yu TK, Bhosale PR, Crane CH, Iyer RB, Skibber JM, Rodriguez-Bigas MA, et al. Patterns of locoregional recurrence after surgery and radiotherapy or chemoradiation for rectal cancer. Int J Radiat Oncol Biol Phys. 2008; 71: 1175-80.
9. Couch DG, Hemingway DM. Complete radiotherapy response in rectal cancer: a review of the evidence. World J Gastroenterol. 2016; 22: 467-70.
10. Levy A, Mercier O, Le Pechoux C. Indications and parameters around postoperative radiation therapy for lung cancer. J Clin Oncol. 2022; 40: 556-66.
11. Trakul N, Harris JP, Le QT, Hara WY, Maxim PG, Loo BW Jr, et al. Stereotactic ablative radiotherapy for reirradiation of locally recurrent lung tumors. J Thorac Oncol. 2012; 7: 1462-5.
12. Xia C, Shi W, Zhang Y, Ding L, Gao L, Wang Q, et al. Prevention and treatment of radiation-induced lung injury. Future Med Chem. 2020; 12: 2161-73.
13. Skeoch S, Weatherley N, Swift AJ, Oldroyd A, Johns C, Hayton C, et al. Drug-induced interstitial lung disease: a systematic review. J Clin Med. 2018; 7: 356.
14. Maher TM. Interstitial lung disease: a review. JAMA. 2024; 331: 1655-65.
15. Frank AJ, Dagogo-Jack I, Dobre IA, Tait S, Schumacher L, Fintelmann FJ, et al. Management of lung cancer in the patient with interstitial lung disease. Oncologist. 2023; 28: 12-22.
16. Wang K, Tepper JE. Radiation therapy-associated toxicity: etiology, management, and prevention. CA Cancer J Clin. 2021; 71: 437-54.
17. Spagnolo P, Distler O, Ryerson CJ, Tzouvelekis A, Lee JS, Bonella F, et al. Mechanisms of progressive fibrosis in connective tissue disease (CTD)-associated interstitial lung diseases (ILDs). Ann Rheum Dis. 2021; 80: 143-50.
18. Reck M, Mellemgaard A. Emerging treatments and combinations in the management of NSCLC: clinical potential of nintedanib. Biologics. 2015; 9: 47-56.
19. Dy GK, Prasad D, Kumar P, Attwood K, Adjei AA. A phase 2 randomized, double-blind, placebo-controlled study evaluating nintedanib versus placebo as prophylaxis against radiation pneumonitis in patients with unresectable NSCLC undergoing chemoradiation therapy. J Thorac Oncol. 2021; 16: e19-20.
20. Tu J, Chen X, Li C, Liu C, Huang Y, Wang X, et al. Nintedanib mitigates radiation-induced pulmonary fibrosis by suppressing epithelial cell inflammatory response and inhibiting fibroblast-to-myofibroblast transition. Int J Biol Sci. 2024; 20: 3353-71.
21. du Bois A, Kristensen G, Ray-Coquard I, Reuss A, Pignata S, Colombo N, et al. Standard first-line chemotherapy with or without nintedanib for advanced ovarian cancer (AGO-OVAR 12): a randomised, double-blind, placebo-controlled phase 3 trial. Lancet Oncol. 2016; 17: 78-89.
22. de Braud F, Cascinu S, Spitaleri G, Pilz K, Clementi L, Liu D, et al. A phase I, dose-escalation study of volasertib combined with nintedanib in advanced solid tumors. Ann Oncol. 2015; 26: 2341-6.
23. Eisen T, Loembe AB, Shparyk Y, MacLeod N, Jones RJ, Mazurkiewicz M, et al. A randomised, phase II study of nintedanib or sunitinib in previously untreated patients with advanced renal cell cancer: 3-year results. Br J Cancer. 2015; 113: 1140-7.

24. Van Cutsem E, Prenen H, D'Haens G, Bennouna J, Carrato A, Ducreux M, et al. A phase I/II, open-label, randomised study of nintedanib plus mFOLFOX6 versus bevacizumab plus mFOLFOX6 in first-line metastatic colorectal cancer patients. Ann Oncol. 2015; 26: 2085-91.
25. Palmer DH, Ma YT, Peck-Radosavljevic M, Ross P, Graham J, Fartoux L, et al. A multicentre, open-label, phase-I/randomised phase-II study to evaluate safety, pharmacokinetics, and efficacy of nintedanib vs. sorafenib in European patients with advanced hepatocellular carcinoma. Br J Cancer. 2018; 118: 1162-8.
26. Tu J, Xu H, Ma L, Li C, Qin W, Chen X, et al. Nintedanib enhances the efficacy of PD-L1 blockade by upregulating MHC-I and PD-L1 expression in tumor cells. Theranostics. 2022; 12: 747-66.
27. Kato R, Haratani K, Hayashi H, Sakai K, Sakai H, Kawakami H, et al. Nintedanib promotes antitumour immunity and shows antitumour activity in combination with PD-1 blockade in mice: potential role of cancer-associated fibroblasts. Br J Cancer. 2021; 124: 914-24.
28. Hilberg F, Roth GJ, Krssak M, Kautschitsch S, Sommergruber W, Tontsch-Grunt U, et al. BIBF 1120: triple angiokinase inhibitor with sustained receptor blockade and good antitumor efficacy. Cancer Res. 2008; 68: 4774-82.
29. Tai WT, Shiau CW, Li YS, Chang CW, Huang JW, Hsueh TT, et al. Nintedanib (BIBF-1120) inhibits hepatocellular carcinoma growth independent of angiokinase activity. J Hepatol. 2014; 61: 89-97.
30. Kutluk Cenik B, Ostapoff KT, Gerber DE, Brekken RA. BIBF 1120 (nintedanib), a triple angiokinase inhibitor, induces hypoxia but not EMT and blocks progression of preclinical models of lung and pancreatic cancer. Mol Cancer Ther. 2013; 12: 992-1001.
31. Laszlo V, Valko Z, Kovacs I, Ozsvar J, Hoda MA, Klikovits T, et al. Nintedanib is active in malignant pleural mesothelioma cell models and inhibits angiogenesis and tumor growth in vivo. Clin Cancer Res. 2018; 24: 3729-40.
32. Widjaja AA, Viswanathan S, Jinrui D, Singh BK, Tan J, Wei Ting JG, et al. Molecular dissection of pro-fibrotic IL11 signaling in cardiac and pulmonary fibroblasts. Front Mol Biosci. 2021; 8: 740650.
33. Liu CY, Huang TT, Chu PY, Huang CT, Lee CH, Wang WL, et al. The tyrosine kinase inhibitor nintedanib activates SHP-1 and induces apoptosis in triple-negative breast cancer cells. Exp Mol Med. 2017; 49: e366.
34. Lee YS, Lee DH, Choudry HA, Bartlett DL, Lee YJ. Ferroptosis-induced endoplasmic reticulum stress: cross-talk between ferroptosis and apoptosis. Mol Cancer Res. 2018; 16: 1073-6.
35. Kellar A, Egan C, Morris D. Preclinical murine models for lung cancer: clinical trial applications. Biomed Res Int. 2015; 2015: 621324.
36. Corbett TH, Griswold DP Jr, Roberts BJ, Peckham JC, Schabel FM Jr. Tumor induction relationships in development of transplantable cancers of the colon in mice for chemotherapy assays, with a note on carcinogen structure. Cancer Res. 1975; 35: 2434-9.
37. Awasthi N, Schwarz MA, Zhang C, Schwarz RE. Augmentation of *nab*-paclitaxel chemotherapy response by mechanistically diverse antiangiogenic agents in preclinical gastric cancer models. Mol Cancer Ther. 2018; 17: 2353-64.
38. Yamanaka T, Harimoto N, Yokobori T, Muranushi R, Hoshino K, Hagiwara K, et al. Nintedanib inhibits intrahepatic cholangiocarcinoma aggressiveness via suppression of cytokines extracted from activated cancer-associated fibroblasts. Br J Cancer. 2020; 122: 986-94.
39. Chen X, Li J, Kang R, Klionsky DJ, Tang D. Ferroptosis: machinery and regulation. Autophagy. 2021; 17: 2054-81.
40. Park E, Chung SW. ROS-mediated autophagy increases intracellular iron levels and ferroptosis by ferritin and transferrin receptor regulation. Cell Death Dis. 2019; 10: 822.
41. Stockwell BR. Ferroptosis turns 10: emerging mechanisms, physiological functions, and therapeutic applications. Cell. 2022; 185: 2401-21.
42. Stockwell BR, Friedmann Angeli JP, Bayir H, Bush AI, Conrad M, Dixon SJ, et al. Ferroptosis: a regulated cell death nexus linking metabolism, redox biology, and disease. Cell. 2017; 171: 273-85.
43. Anandhan A, Dodson M, Schmidlin CJ, Liu P, Zhang DD. Breakdown of an ironclad defense system: the critical role of NRF2 in mediating ferroptosis. Cell Chem Biol. 2020; 27: 436-47.
44. Wang L, Liu Y, Du T, Yang H, Lei L, Guo M, et al. ATF3 promotes erastin-induced ferroptosis by suppressing system $Xc^-$. Cell Death Differ. 2020; 27: 662-75.
45. Jiang L, Kon N, Li T, Wang SJ, Su T, Hibshoosh H, et al. Ferroptosis as a p53-mediated activity during tumour suppression. Nature. 2015; 520: 57-62.
46. Kilberg MS, Shan J, Su N. ATF4-dependent transcription mediates signaling of amino acid limitation. Trends Endocrinol Metab. 2009; 20: 436-43.
47. Gao R, Kalathur RKR, Coto-Llerena M, Ercan C, Buechel D, Shuang S, et al. YAP/TAZ and ATF4 drive resistance to Sorafenib in hepatocellular carcinoma by preventing ferroptosis. EMBO Mol Med. 2021; 13: e14351.
48. Koppula P, Zhuang L, Gan B. Cystine transporter SLC7A11/xCT in cancer: ferroptosis, nutrient dependency, and cancer therapy. Protein Cell. 2021; 12: 599-620.
49. He F, Zhang P, Liu J, Wang R, Kaufman RJ, Yaden BC, et al. ATF4 suppresses hepatocarcinogenesis by inducing SLC7A11 (xCT) to block stress-related ferroptosis. J Hepatol. 2023; 79: 362-77.
50. Huang N, Liu Y, Fang Y, Zheng S, Wu J, Wang M, et al. Gold nanoparticles induce tumor vessel normalization and impair metastasis by inhibiting endothelial Smad2/3 signaling. ACS Nano. 2020; 14: 7940-58.
51. Efimova I, Catanzaro E, Van der Meeren L, Turubanova VD, Hammad H, Mishchenko TA, et al. Vaccination with early ferroptotic cancer cells induces efficient antitumor immunity. J Immunother Cancer. 2020; 8: e001369.
52. Chen DS, Irving BA, Hodi FS. Molecular pathways: next-generation immunotherapy—inhibiting programmed death-ligand 1 and programmed death-1. Clin Cancer Res. 2012; 18: 6580-7.

53. Lei G, Zhang Y, Koppula P, Liu X, Zhang J, Lin SH, et al. The role of ferroptosis in ionizing radiation-induced cell death and tumor suppression. Cell Res. 2020; 30: 146-62.
54. Ye LF, Chaudhary KR, Zandkarimi F, Harken AD, Kinslow CJ, Upadhyayula PS, et al. Radiation-induced lipid peroxidation triggers ferroptosis and synergizes with ferroptosis inducers. ACS Chem Biol. 2020; 15: 469-84.
55. Lang X, Green MD, Wang W, Yu J, Choi JE, Jiang L, et al. Radiotherapy and immunotherapy promote tumoral lipid oxidation and ferroptosis via synergistic repression of SLC7A11. Cancer Discov. 2019; 9: 1673-85.
56. Huang L, Bin L, Hu Hu Z. AGAP2-AS1 affects TNM staging and prognosis of lung cancer patients by acting on SLC7A11 mRNA stability and ferroptosis. Oncol Transl Med. 2023; 9: 115-20.
57. Zhang S, Zhang J, Fan X, Liu H, Zhu M, Yang M, et al. Ionizing radiation-induced ferroptosis based on nanomaterials. Int J Nanomedicine. 2022; 17: 3497-507.
58. Lei G, Mao C, Yan Y, Zhuang L, Gan B. Ferroptosis, radiotherapy, and combination therapeutic strategies. Protein Cell. 2021; 12: 836-57.
59. Awasthi N, Hinz S, Brekken RA, Schwarz MA, Schwarz RE. Nintedanib, a triple angiokinase inhibitor, enhances cytotoxic therapy response in pancreatic cancer. Cancer Lett. 2015; 358: 59-66.
60. Jamadar A, Suma SM, Mathew S, Fields TA, Wallace DP, Calvet JP, et al. The tyrosine-kinase inhibitor Nintedanib ameliorates autosomal-dominant polycystic kidney disease. Cell Death Dis. 2021; 12: 947.
61. Cho HJ, Hwang JA, Yang EJ, Kim EC, Kim JR, Kim SY, et al. Nintedanib induces senolytic effect via STAT3 inhibition. Cell Death Dis. 2022; 13: 760.
62. Liang C, Zhang X, Yang M, Dong X. Recent progress in ferroptosis inducers for cancer therapy. Adv Mater. 2019; 31: e1904197.
63. Mou Y, Wang J, Wu J, He D, Zhang C, Duan C, et al. Ferroptosis, a new form of cell death: opportunities and challenges in cancer. J Hematol Oncol. 2019; 12: 34.
64. Liu Y, Pi F, He L, Yang F, Chen T. Oxygen vacancy-rich manganese nanoflowers as ferroptosis inducers for tumor radiotherapy. Small. 2024: e2310118.
65. Lin Y, Chen X, Yu C, Xu G, Nie X, Cheng Y, et al. Radiotherapy-mediated redox homeostasis-controllable nanomedicine for enhanced ferroptosis sensitivity in tumor therapy. Acta Biomater. 2023; 159: 300-11.
66. Liu S, Zhang HL, Li J, Ye ZP, Du T, Li LC, et al. Tubastatin A potently inhibits GPX4 activity to potentiate cancer radiotherapy through boosting ferroptosis. Redox Biol. 2023; 62: 102677.
67. Lin Z, Yang S, Qiu Q, Cui G, Zhang Y, Yao M, et al. Hypoxia-induced cysteine metabolism reprogramming is crucial for the tumorigenesis of colorectal cancer. Redox Biol. 2024; 75: 103286.
68. Wortel IMN, van der Meer LT, Kilberg MS, van Leeuwen FN. Surviving stress: modulation of ATF4-mediated stress responses in normal and malignant cells. Trends Endocrinol Metab. 2017; 28: 794-806.
69. Pan L, Cheng Y, Yang W, Wu X, Zhu H, Hu M, et al. Nintedanib ameliorates bleomycin-induced pulmonary fibrosis, inflammation, apoptosis, and oxidative stress by modulating PI3K/Akt/mTOR pathway in mice. Inflammation. 2023; 46: 1531-42.
70. Tabata S, Kojima Y, Sakamoto T, Igarashi K, Umetsu K, Ishikawa T, et al. L-2hydroxyglutaric acid rewires amino acid metabolism in colorectal cancer via the mTOR-ATF4 axis. Oncogene. 2023; 42: 1294-307.
71. Park Y, Reyna-Neyra A, Philippe L, Thoreen CC. mTORC1 balances cellular amino acid supply with demand for protein synthesis through post-transcriptional control of ATF4. Cell Rep. 2017; 19: 1083-90.
72. Cao T, Zhang W, Wang Q, Wang C, Ma W, Zhang C, et al. Cancer SLC6A6-mediated taurine uptake transactivates immune checkpoint genes and induces exhaustion in $CD8^+$ T cells. Cell. 2024; 187: 2288-304.e2227.
73. Selvarajah B, Azuelos I, Plate M, Guillotin D, Forty EJ, Contento G, et al. mTORC1 amplifies the ATF4-dependent de novo serine-glycine pathway to supply glycine during TGF-$\beta_1$-induced collagen biosynthesis. Sci Signal. 2019; 12: eaav3048.
74. Tang R, Xu J, Zhang B, Liu J, Liang C, Hua J, et al. Ferroptosis, necroptosis, and pyroptosis in anticancer immunity. J Hematol Oncol. 2020; 13: 110.
75. Ameri K, Harris AL. Activating transcription factor 4. Int J Biochem Cell Biol. 2008; 40: 14-21.
76. Kim EJ, Lee YJ, Kang S, Lim YB. Ionizing radiation activates PERK/eIF2α/ATF4 signaling via ER stress-independent pathway in human vascular endothelial cells. Int J Radiat Biol. 2014; 90: 306-12.


**Cite this article as:** Li C, Aili A, Yu Q, Yang M, Feng Q, Xu D, et al. Nintedanib enhances tumor cell radiosensitivity by promoting ferroptosis and modulating the ATF4/SLC7A11/GSH axis. Cancer Biol Med. 2025; 22: 1627-1647. doi: 10.20892/j.issn.2095-3941.2025.0275